

Comparing quasiparticle H₂O level alignment on anatase and rutile TiO₂

Huijuan Sun,^{†,‡} Duncan J. Mowbray,^{*,‡} Annapaola Migani,^{¶,§} Jin Zhao,^{†,||,⊥} Hrvoje Petek,[#] and Angel Rubio^{‡,⊗}

[†]Hefei National Laboratory for Physical Sciences at the Microscale, University of Science and Technology of China, Hefei, Anhui 230026, China.

[‡]Nano-Bio Spectroscopy Group and ETSF Scientific Development Center, Departamento de Física de Materiales, Centro de Física de Materiales CSIC-UPV/EHU-MPC and DIPC, Universidad del País Vasco UPV/EHU, E-20018 San Sebastián, Spain

[¶]ICN2 - Institut Català de Nanociència i Nanotecnologia, ICN2 Building, Campus UAB, E-08193 Bellaterra (Barcelona), Spain

[§]CSIC - Consejo Superior de Investigaciones Científicas, ICN2 Building, Campus UAB, E-08193 Bellaterra (Barcelona), Spain

^{||}Department of Physics and ICQD, University of Science and Technology of China, Hefei, Anhui 230026, China

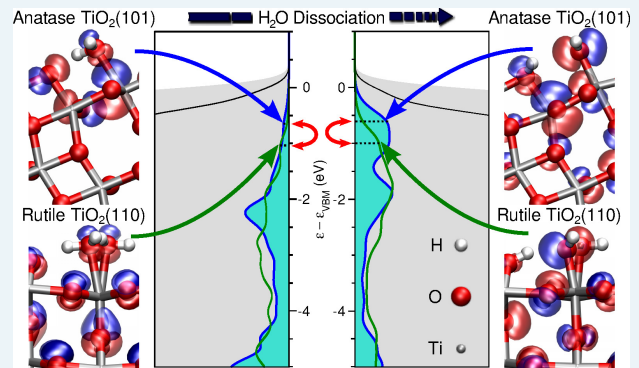
[⊥]Synergetic Innovation Center of Quantum Information & Quantum Physics, University of Science and Technology of China, Hefei, Anhui 230026, China

[#]Department of Physics and Astronomy, University of Pittsburgh, Pittsburgh, Pennsylvania 15260, USA

[⊗]Max Planck Institute for the Structure and Dynamics of Matter, Luruper Chaussee 149, D-22761 Hamburg, Germany

ABSTRACT: Knowledge of the molecular frontier levels' alignment in the ground state can be used to predict the photocatalytic activity of an interface. The position of the adsorbate's highest occupied molecular orbital (HOMO) levels relative to the substrate's valence band maximum (VBM) in the interface describes the favorability of photogenerated hole transfer from the VBM to the adsorbed molecule. This is a key quantity for assessing and comparing H₂O photooxidation activities on two prototypical photocatalytic TiO₂ surfaces: anatase (A)-TiO₂(101) and rutile (R)-TiO₂(110). Using the projected density of states (DOS) from state-of-the-art quasiparticle (QP) G_0W_0 calculations, we assess the relative photocatalytic activity of intact and dissociated H₂O on coordinately unsaturated (Ti_{cus}) sites of idealized stoichiometric A-TiO₂(101)/R-TiO₂(110) and bridging O vacancies (O_{br}^{vac}) of defective A-TiO_{2-x}(101)/R-TiO_{2-x}(110) surfaces ($x = 1/4, 1/8$) for various coverages. Such a many-body treatment is necessary to correctly describe the anisotropic screening of electron-electron interactions at a photocatalytic interface, and hence obtain accurate interfacial level alignments. The more favorable ground state HOMO level alignment for A-TiO₂(101) may explain why the anatase polymorph shows higher photocatalytic activities than the rutile polymorph. Our results indicate that (1) hole trapping is more favored on A-TiO₂(101) than R-TiO₂(110) and (2) HO@ Ti_{cus} is more photocatalytically active than intact H₂O@ Ti_{cus} .

KEYWORDS: water splitting, G_0W_0 calculations, photocatalysis, photooxidation, hole trapping, titania



1. INTRODUCTION

TiO₂ is widely used in photocatalysis, photoelectrocatalysis, and photovoltaics.¹⁻⁶ In particular, the H₂O-TiO₂ interface has been intensively studied both experimentally⁷ and theoretically.⁸ This is due to both the ubiquitous nature of the aqueous environment, and the technological importance of water splitting.^{9,10} Because large single-crystal samples of the anatase polymorph are less stable than the rutile polymorph,¹¹⁻¹³ most surface science studies have focused on the rutile (110) surface of TiO₂. However, in the nanoparticle form the anatase polymorph is more stable,¹⁴ and moreover it has a higher photocatalytic activity.¹⁵

A proper assessment of an interface's photocatalytic activity requires an accurate description of its frontier levels' alignment. This is because interfacial electron transfer is controlled by the alignment of the highest occupied and lowest unoccupied molecular orbitals (HOMO/LUMO) relative to the valence band maximum (VBM) and conduction band minimum (CBM).^{4,5} In particular,

H₂O photooxidation, i.e., the oxygen evolution reaction (OER), is initiated by the transfer of the photogenerated hole from the substrate's VBM to the HOMO.¹⁶⁻¹⁸

Based on the HOMO's position relative to the VBM prior to irradiation, i.e., vertical alignment, one may establish trends in photocatalytic activity among a group of systems.^{19,20} Even in cases where the HOMO initially lies below the VBM,²¹ after light absorption and nuclear relaxation, these levels may reorder, with the hole localized on the molecule.²² Essentially, the closer to the VBM and more localized on the molecule the HOMO is initially, the greater the molecule's propensity for trapping the hole. For these reasons, the alignment of the H₂O occupied levels prior to irradiation is most relevant for understanding the OER.

Recently, we applied many-body quasiparticle (QP) GW techniques^{23,24} to determine the H₂O occupied levels' alignment on rutile (R)-TiO₂(110).²¹ We found that an accurate description of the interfacial anisotropic screening via QP GW is essential to ac-

curately describe the interfacial level alignment.^{21,25–27} Specifically, the occupied QP density of states (DOS) projected onto the molecule is an effective means for interpreting difference spectra, i.e., the difference between spectra with a chemisorbed molecular overlayer and a clean TiO₂ surface, from ultraviolet photoemission spectroscopy (UPS).²¹ Such theoretical approaches are necessary to disentangle highly hybridized adsorbate levels from those of the substrate, such as those of the H₂O–TiO₂ interface.²¹

Here, we investigate the H₂O occupied levels’ alignment on the anatase (A)-TiO₂(101) surface, as it is the most common surface in nanostructured TiO₂.^{2,28,29} In the absence of UPS measurements for H₂O on A-TiO₂(101), we compare the results to the G_0W_0 PDOS of H₂O on R-TiO₂(110),³⁰ which is consistent with UPS difference spectra.^{31–33}

In particular, we perform G_0W_0 ^{23,24,34} and partially self-consistent³⁵ (sc)QP GW¹^{25,26} calculations based on Kohn-Sham (KS) levels from density functional theory (DFT) using a local density approximation (LDA),³⁶ generalized gradient approximation (PBE)³⁷, or a range-separated hybrid (HSE)^{38,39} exchange correlation (xc)-functionals. From these calculations we obtain the total and projected QP DOS for a variety of coverages [$\frac{1}{4}$ to $1\frac{1}{2}$ monolayer (ML)] of intact and dissociated H₂O adsorbed on coordinately unsaturated Ti sites (H₂O@Ti_{cus}) of stoichiometric A-TiO₂(101) and bridging O vacancies (H₂O@O_{br}^{vac}) of defective A-TiO_{2– $\frac{1}{4}$} (101) and A-TiO_{2– $\frac{1}{8}$} (101) surfaces with $\frac{1}{2}$ ML and $\frac{1}{4}$ ML O_{br}^{vac}. The Ti_{cus} and O_{br} sites of A-TiO₂(101) and R-TiO₂(110) are shown schematically in Figure 1.

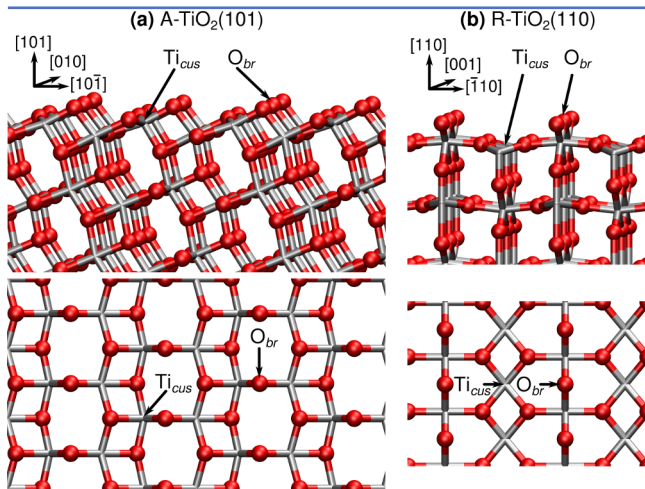


Figure 1. Schematics of clean stoichiometric (a) A-TiO₂(101) and (b) R-TiO₂(110) surfaces. Ti and O atoms are depicted in silver and red, respectively. Coordinately unsaturated Ti sites (Ti_{cus}) and bridging O atoms (O_{br}) are labelled.

On the one hand, by considering the absolute interfacial level alignment, i.e., relative to the vacuum level E_{vac} , one obtains the interface’s ionization potential $IP = -\epsilon_{VBM} + E_{vac}$. This is the quantity that can be compared with red-ox potentials.^{40,41} Moreover, the absolute level alignment allows a direct comparison between alignments across different substrates,²⁰ such as A-TiO₂(101) and R-TiO₂(110). Finally, from the absolute level alignment, one can determine whether changes in the H₂O level alignment across different substrates are attributable to shifts of the substrate or molecular levels.

On the other hand, by considering the level alignment relative to the VBM of the substrate ϵ_{VBM} , one may directly compare the favorability of photogenerated hole transfer from the substrate’s VBM to the molecule’s HOMO. In combination with the IP this allows a robust comparison of photocatalytic activity across sub-

strates. Moreover, by referencing the spectra to the VBM, one may directly compare the shape and dispersion of the valence band edge at the VBM. Finally, the VBM is the most reliable KS energy reference, from a theoretical perspective.²⁶

For these reasons, we shall make use of both VBM and E_{vac} energy references as appropriate. In particular, we provide the absolute level alignment when comparing to HSE DFT and HSE G_0W_0 DOS. This is because the VBM and CBM from HSE DFT for clean²⁶ and 1ML H₂O@Ti_{cus}^{21,40,41} on R-TiO₂(110) are consistent with measurements for clean quasi-stoichiometric^{26,42–45} and liquid H₂O covered R-TiO₂(110),⁴¹ respectively.

We begin by providing a detailed description of the techniques, parameters, and terminology employed throughout in Section 2. In Section 3.1 we compare our results to calculated and measured electronic band gaps E_g , optical band gaps $\hbar\omega_g$, and macroscopic dielectric constants ϵ_∞ of bulk A-TiO₂ and R-TiO₂ available in the literature. To further test the robustness of our approach, and the parameters employed, we compare the dielectric function obtained by solving the Bethe-Salpeter equation (BSE) based on G_0W_0 eigenvalues with that obtained from reflection spectra measurements for bulk A-TiO₂. We also compare the IP for clean idealized stoichiometric A-TiO₂(101) and R-TiO₂(110). In Section 3.2 we provide a detailed comparison of the H₂O PDOS for intact and $\frac{1}{2}$ dissociated H₂O@Ti_{cus} on A-TiO₂(101) and R-TiO₂(110) relative to E_{vac} and ϵ_{VBM} with PBE DFT, HSE DFT, PBE scQP GW¹, PBE G_0W_0 and HSE G_0W_0 . In Section 3.3 we provide a similar detailed comparison for dissociatively adsorbed H₂O@O_{br}^{vac} on A-TiO_{2– $\frac{1}{4}$} (101) and R-TiO_{2– $\frac{1}{4}$} (110) relative to E_{vac} . Finally, in Section 3.4 we extend the comparison of A-TiO₂(101) and R-TiO₂(110) to their adsorption energies and level alignments relative to ϵ_{VBM} with H₂O coverage ($\frac{1}{4}$ to $1\frac{1}{2}$ ML), H₂O dissociation (intact to fully dissociated), and surface composition (O_{br}^{vac} coverage). This is followed by concluding remarks.

2. METHODOLOGY

2.1. Theoretical Methods. DFT based on standard xc-functionals, e.g., LDA and PBE, tends to significantly underestimate the electronic band gaps of semiconducting metal oxides, such as TiO₂.⁴⁶ This is in part due to their underestimation of the screening of the electron-electron interaction.

DFT based on hybrid xc-functionals, e.g., HSE, partially remedies this by replacing a fraction of the exchange term with Hartree-Fock exact-exchange. The fraction of Hartree-Fock exact-exchange included, α , acts as an effective constant screening of the Hartree-Fock electron-electron interaction term, i.e., an inverse dielectric constant for the system $\alpha \sim \epsilon_\infty^{-1}$.⁴⁷ In particular, we use the HSE06 variant, with a range separation parameter of $\mu = 0.2 \text{ \AA}^{-1}$, of the HSE hybrid xc-functional, which includes 25% exact-exchange ($\alpha = 0.25$).³⁸ For systems where the screening is rather homogeneous, and $\epsilon_\infty \sim 4$, this leads to a better description of the electronic band gap,⁴⁷ e.g., of bulk TiO₂.⁴⁶

However, since HSE applies the same screening to all the levels regardless of their nature, it fails to describe the anisotropic screening felt by molecular levels at an interface. As a result, localized occupied molecular levels are underbound by HSE.^{21,25,26} This can lead to significant errors in HSE’s description of molecular/semiconductor interfacial level alignment.^{21,25,26} Instead, QP techniques, e.g., G_0W_0 and scQP GW¹, where the spacial dependence of the screening is explicitly included, provide a better description of the interfacial level alignment.^{21,25–27}

In the G_0W_0 approach, the contribution to the KS eigenvalues from the xc-potential V_{xc} is replaced by the self energy $\Sigma = iGW$, where G is the Green’s function and W is the spatially depen-

dent screening²³ obtained from the KS wavefunctions.²⁴ The dielectric function is obtained from linear response time-dependent (TD) DFT within the random phase approximation (RPA), including local field effects.³⁴ From G_0W_0 one obtains first-order QP corrections to the KS eigenvalues, but retains the KS wavefunctions. Generally, these QP corrections to the occupied levels are linearly dependent on the fraction of the KS wavefunction's density in the molecular layer.^{25,26} This means the screening of these levels W is quite anisotropic. For this reason, QP GW methods are necessary to accurately describe the interfacial level alignment.

Moreover, to include dependencies on the QP wavefunctions, and possibly obtain an improved absolute level alignment for the interface, one can also employ self-consistent QP techniques, such as scQPGW1.^{21,25,26} Here, we have employed a single-shot scQPGW1 approach,^{25,35} where 100% of the DFT xc-potential is replaced by the QP self energy in a single self-consistent scQPGW cycle. We employ this procedure to make practical scQPGW calculations for large interfaces, such as H_2O -A-TiO₂(101). In so doing, one obtains eigenvalues comparable to those from G_0W_0 , along with the QP wavefunctions. This differs from the scQPGW1 approach as previously applied to the H_2O -R-TiO₂(110) interface,²¹ where 25%, 25%, and 50%, of the QP self energies were "mixed" with the DFT xc-potential over three scQPGW cycles,³⁵ respectively.

2.2. Computational Details. Our G_0W_0 calculations^{23,24,34} have been performed using *vasp* within the projector augmented wave (PAW) scheme.⁴⁸ The G_0W_0 calculations are based on KS wavefunctions and eigenenergies obtained from DFT using either LDA,³⁶ PBE,³⁷ or HSE³⁸ xc-functionals.⁴⁹

The geometries have been fully relaxed using LDA³⁶ or PBE,³⁷ with all forces $\lesssim 0.02$ eV/Å. The HSE³⁸ calculations have been performed for the relaxed geometries obtained with PBE. We have employed a plane-wave energy cutoff of 445 eV, an electronic temperature of $k_B T \approx 0.1$ eV with all energies extrapolated to $T \rightarrow 0$ K, and a PAW pseudopotential for Ti which includes the $3s^2$ and $3p^6$ semi-core levels. All calculations have been performed spin unpolarized.²¹

For the clean stoichiometric A-TiO₂(101) surface we have used a five-layer slab, an orthorhombic 1×1 unit cell of $10.23 \times 3.78 \times 40$ Å³, a Γ -centered $4 \times 8 \times 1$ \mathbf{k} -point mesh, and approximately 9 $\frac{1}{3}$ unoccupied bands per atom. For the clean defective A-TiO_{2- x} (101) surface we have used a monoclinic 1×2 unit cell of $10.23 \times 7.56 \times 40$ Å³ and a Γ -centered $4 \times 4 \times 1$ \mathbf{k} -point mesh. For the clean defective A-TiO_{2- $\frac{1}{6}$} (101) surface we have used a 1×4 unit cell of $10.23 \times 15.13 \times 40$ Å³ and a Γ -centered $4 \times 2 \times 1$ \mathbf{k} -point mesh. For the H_2O covered surfaces, we have employed a five-layer slab with adsorbates on both sides, an orthorhombic 1×1 unit cell of $10.23 \times 3.78 \times 47$ Å³, a Γ centered $4 \times 8 \times 1$ \mathbf{k} -point mesh, and approximately 9% unoccupied bands per atom, i.e., including all levels up to 30 eV above the VBM, an energy cutoff of 80 eV for the number of \mathbf{G} -vectors, and a sampling of 80 frequency points for the RPA dielectric function. The G_0W_0 parameters are consistent with those previously used for describing bulk R-TiO₂, R-TiO₂(110) clean surface and interfaces.^{25,26} Although our G_0W_0 calculations do not include electron-phonon⁵⁰ and lattice polarization⁵¹ contributions, these parameters have been shown to provide accurate descriptions of bulk optical absorption spectra, and both clean surface and interfacial level alignment.^{25,26}

It has previously been shown^{46,52,53} that the experimental optical spectra for bulk A-TiO₂ may be obtained via BSE⁵⁴ based on G_0W_0 eigenvalues. In our BSE calculations, we include the electrostatic electron-hole interaction using the effective nonlocal frequency independent exchange correlation $f_{xc}(\mathbf{r}, \mathbf{r}', \omega = 0)$ kernel suggested in ref. 55. For bulk A-TiO₂, we have used a tetrago-

nal conventional 12 atom supercell with experimental lattice parameters $a = b = 3.78$ Å and $c = 9.5$ Å,⁵⁶ and a dense Γ -centered $10 \times 10 \times 4$ \mathbf{k} -point mesh. For bulk R-TiO₂, we have used a tetragonal 6 atom primitive cell with experimental lattice parameters $a = b = 4.5941$ Å and $c = 2.958$ Å,⁵⁶ a Γ -centered $6 \times 6 \times 10$ \mathbf{k} -point mesh with PBE and HSE and a denser Γ -centered $8 \times 8 \times 12$ \mathbf{k} -point mesh with LDA. For both A-TiO₂ and R-TiO₂, we have included $n_{\text{unocc}} = 12$ unoccupied bands per atom. For the BSE calculations of bulk A-TiO₂, we have used 480 sampling points for the RPA dielectric function, and included all the transitions between the 16 highest energy occupied bands and the 12 lowest energy unoccupied bands.⁵⁴

2.3. Terminology. To compare the relative stabilities of the H_2O covered anatase and rutile polymorphs, we have performed single-point RPBE⁵⁷ based DFT calculations using the PBE relaxed structure for the H_2O adsorption energies E_{ads} on stoichiometric A-TiO₂(101) and defective A-TiO_{2- x} (101) surfaces. The RPBE xc-functional was especially developed for the prediction of adsorption properties on metal surfaces.⁵⁷ Furthermore, RPBE has been shown to provide accurate formation energies for metal dioxides⁵⁸ and perovskites.⁵⁹

The H_2O adsorption energy on the Ti_{cus} site of a stoichiometric A-TiO₂(101) surface is given by

$$E_{\text{ads}} \approx \frac{E[nH_2O + A\text{-TiO}_2(101)] - E[A\text{-TiO}_2(101)]}{n} - E[H_2O], \quad (1)$$

where n is the number of adsorbed H_2O functional units in the supercell, and $E[nH_2O + A\text{-TiO}_2(101)]$, $E[A\text{-TiO}_2(101)]$, and $E[H_2O]$ are the total energies of the covered and clean stoichiometric surfaces and gas phase water molecule, respectively. Similarly, the H_2O adsorption energy on the $O_{\text{br}}^{\text{vac}}$ site of a defective A-TiO_{2- x} (101) surface is given by

$$E_{\text{ads}} \approx \frac{E[nH_2O + A\text{-TiO}_{2-x}(101)] - E[A\text{-TiO}_{2-x}(101)]}{n} - E[H_2O], \quad (2)$$

where $E[nH_2O + A\text{-TiO}_{2-x}(101)]$ and $E[A\text{-TiO}_{2-x}(101)]$ are the total energies of the covered and clean defective surfaces, respectively.

To provide a quantitative comparison between the DOS for the H_2O -A-TiO₂ and H_2O -R-TiO₂ interfaces, we employ the interfaces' IP s. These are obtained from the difference in energy between the vacuum level E_{vac} and the VBM ε_{VBM} , $IP = -\varepsilon_{\text{VBM}} + E_{\text{vac}}$, where E_{vac} is the maximum surface averaged electrostatic potential in the vacuum region between slabs.

Similarly, to provide a quantitative comparison between the PDOS for the H_2O -A-TiO₂ and H_2O -R-TiO₂ interfaces, we employ both the highest H_2O PDOS peak $\varepsilon_{\text{peak}}^{\text{PDOS}}$ and the average energy of the highest energy electron, or HOMO, of the PDOS, $\varepsilon_{\text{HOMO}}^{\text{PDOS}}$. To obtain $\varepsilon_{\text{peak}}^{\text{PDOS}}$ from the PDOS, we fit three Gaussians to the first few peaks below the VBM. In this way we may disentangle the highest energy peak when it forms a shoulder within the upper edge of the PDOS.

However, to assess trends in the comparative photocatalytic activity of the H_2O -A-TiO₂ and H_2O -R-TiO₂ interfaces, one should consider not only a peak's energy, but also differences in its' intensity, i.e., localization on H_2O . Both quantities are incorporated within the single descriptor $\varepsilon_{\text{HOMO}}^{\text{PDOS}}$. We define $\varepsilon_{\text{HOMO}}^{\text{PDOS}}$ as the first moment of the PDOS, $\rho^{\text{PDOS}}(\varepsilon)$ over the interval encompassing the highest energy electron. More precisely,

$$\varepsilon_{\text{HOMO}}^{\text{PDOS}} \equiv \int_{E_1}^{\varepsilon_{\text{VBM}} + \Delta} \varepsilon \rho^{\text{PDOS}}(\varepsilon) d\varepsilon, \quad (3)$$

where ε_{VBM} is the VBM energy, $\Delta \sim 1$ eV ensures the tail of the VBM is included within the integral, and E_1 is the lower bound of

the energy range encompassing the highest energy electron of the PDOS, i.e.,

$$\int_{E_1}^{\varepsilon_{\text{VBM}+\Delta}} \rho^{\text{PDOS}}(\varepsilon) d\varepsilon \equiv 1. \quad (4)$$

3. RESULTS AND DISCUSSION

3.1. Bulk and (101) Surface of Anatase TiO₂. To test the reliability of the parameters we have employed to calculate the G_0W_0 levels of A-TiO₂, we first consider the optical response of bulk anatase. Previous DFT band structure calculations^{46,52,53} found A-TiO₂ has an indirect electronic band gap between the VBM along the Σ path at $0.88\Gamma \rightarrow M^{46}$, i.e., Σ , and the CBM at Γ . Our PBE G_0W_0 calculation yields an indirect electronic band gap for A-TiO₂ of 3.86 eV, from a VBM at $0.8\Gamma \rightarrow M$. This is comparable with the G_0W_0 indirect band gaps reported in the literature, as shown in Table 1.

Table 1. Direct and Indirect Band Gaps E_g and Optical Gaps $\hbar\omega_g$ in eV of A-TiO₂ and R-TiO₂.

method	xc-functional	A-TiO ₂		R-TiO ₂	
		$\Gamma \rightarrow \Gamma$	$\Sigma \rightarrow \Gamma$	$\Gamma \rightarrow \Gamma$	$\Gamma \rightarrow R$
electronic band gap					
DFT	HSE	3.72	3.63	3.40	3.40
			3.60 ^a	3.39 ^a	3.39 ^a
	LDA	3.93	3.86	3.33	3.26
		4.14 ^b	3.56 ^b	3.38 ^b	3.34 ^b
G_0W_0	PBE		3.73 ^a	3.46 ^a	
		4.29 ^c	3.83 ^c	3.59 ^c	
	PBE+ Δ		3.57 ^d	3.30 ^d	3.23 ^d
PES/IPES ($\alpha_{\text{KM}} \cdot \hbar\omega$) ²				3.3 \pm 0.5 ^e	
		3.53 ^f		3.37 ^f	
optical gap					
BSE	LDA	3.73		3.15	
	PBE	3.57 ^a		3.28 ^a	
Transmission		3.42 ^g			
Absorption				3.03 ^h	
Reflectance		3.21 ⁱ		3.00 ⁱ	

^aRef. 46. ^bRef. 53. ^cRef. 52. ^dRef. 60. ^ePhotoemission and Bremsstrahlung isochromat spectroscopy from ref. 61. ^fEstimate assuming a nearly direct band gap based on Kubelka-Munk adsorption coefficients α_{KM} from reflectance measurements of phase-pure nanoparticles in ref. 62. ^gRef. 63. ^hRefs. 64 and 65. ⁱFor pure-phase nanoparticles from ref. 62.

Based on these G_0W_0 levels, we obtain from the Bethe-Salpeter equation the imaginary and real parts of the dielectric function of bulk A-TiO₂ for polarization perpendicular (ordinary) and parallel (extraordinary) to the tetragonal axis c shown in Figure 2. These are comparable to the dielectric functions obtained from reflection spectra polarized perpendicular to the a or c -axis at room temperature by Kramers-Kronig transformations.⁶⁶ Note that 86% of the experimental reflectivity spectra polarized perpendicular to the a -axis is parallel to the c -axis.⁶⁶ Furthermore, our dielectric functions agree well with those obtained from BSE calculations within the Tamm-Dancoff approximation.⁴⁶ In particular, we obtain excellent agreement both in position and intensity for the first bright exciton at ~ 4 eV, which is perpendicular to the c -axis. The lowest energy BSE G_0W_0 transition is at 3.73 eV, about 0.12 eV below the PBE G_0W_0 indirect electronic gap of A-TiO₂, as shown in Table 1. This is significantly higher than the estimated optical band gap of 3.42 eV reported in ref. 63.

However, we tend to underestimate the real part of the dielectric function, shown in Figure 2(b,d). For example, as reported in Table 2, the dielectric constant $\varepsilon_\infty = \varepsilon(\omega = 0)$ is underestimated by about 2 in our BSE calculations. This might be remedied by including a greater number of transitions within the BSE calculation.

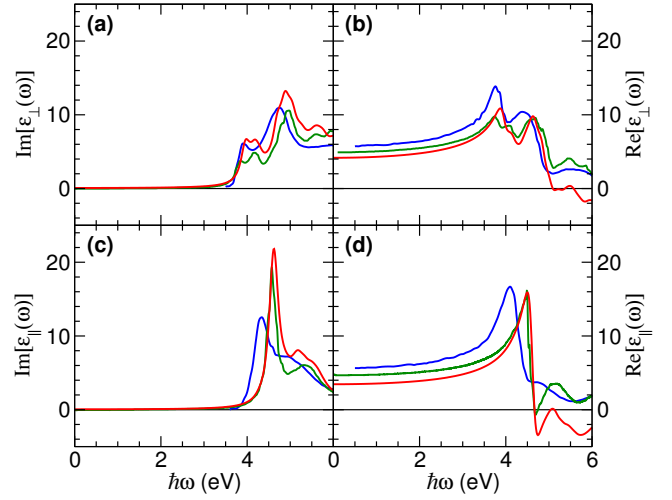


Figure 2. (a,c) Imaginary and (b,d) real parts of the dielectric function of bulk A-TiO₂ for polarization perpendicular (a,b) and parallel (c,d) to the A-TiO₂ tetragonal c -axis, $\text{Im}[\varepsilon_{\perp}(\omega)]$, $\text{Re}[\varepsilon_{\perp}(\omega)]$, $\text{Im}[\varepsilon_{\parallel}(\omega)]$, and $\text{Re}[\varepsilon_{\parallel}(\omega)]$, versus energy ($\hbar\omega_g$), in eV. The BSE spectra from this work (red) and from ref. 46 (green) are based on G_0W_0 eigenvalues. The experimental spectra (blue) are obtained from reflection spectra polarized perpendicular to the (a,b) c -axis or (c,d) a -axis by Kramers-Kronig transformation from Ref. 66.

Table 2. Macroscopic Dielectric Constants ε_∞ Perpendicular (\perp) and Parallel (\parallel) to the Tetragonal c -axis of A-TiO₂ and R-TiO₂.

method	xc-functional	A-TiO ₂		R-TiO ₂	
		\perp	\parallel	\perp	\parallel
DFT	LDA	7.18	6.81	7.83 ^a	9.38 ^a
				7.69 ^b	8.91 ^b
RPA	PBE	7.06	6.60	7.61	9.09
				7.55 ^b	9.02 ^b
BSE- G_0W_0	LDA	4.91	4.83	5.21	6.09
				5.74 ^b	6.77 ^b
BSE- G_0W_0	PBE	4.17	3.45	5.60 ^a	7.11 ^a
		4.91 ^c	4.76 ^c	5.15 ^c	6.22 ^c
BSE-DFT	PBE+ Δ	5.12 ^d	4.98 ^d	5.71 ^d	7.33 ^d
				5.79 ^e	7.04 ^e
Experiment		5.73 ^f	5.64 ^f	5.88 ^g	7.14 ^g
				6.84 ^h	8.43 ^h

^aRef. 26. ^bRef. 67. ^cRef. 46. ^dRef. 60. ^eRef. 68. ^fRef. 66. ^gRef. 69. ^hRef. 70.

In any case, such computationally demanding calculations are beyond the scope of the present work. Overall, the agreement obtained for the BSE dielectric function based on G_0W_0 eigenenergies demonstrates the robustness of the parameters we will use to calculate the G_0W_0 PDOS for H₂O.

Figure 1 depicts schematically the clean and stoichiometric A-TiO₂(101) surface. For the clean surface, there are two Ti coordinately unsaturated sites (Ti_{cus}) and two bridging O atoms (O_{br}) in each unit cell.

PBE G_0W_0 places the IP for A-TiO₂(101) at 7.15 eV, which is 0.14 eV below that of R-TiO₂(110).²⁶ This relative ordering is consistent with, albeit significantly smaller than, that measured with XPS for the A-TiO₂-RuO₂-R-TiO₂ interface of 0.7 ± 0.1 eV.⁷² This ordering also agrees with the 0.47 eV difference in IP calculated using a hybrid quantum-mechanical/molecular mechanical embedding technique.⁷³ In these calculations the IP was obtained from the total energy difference upon removal of an electron from the neutral A-TiO₂ and R-TiO₂ embedded cluster models. Our rela-

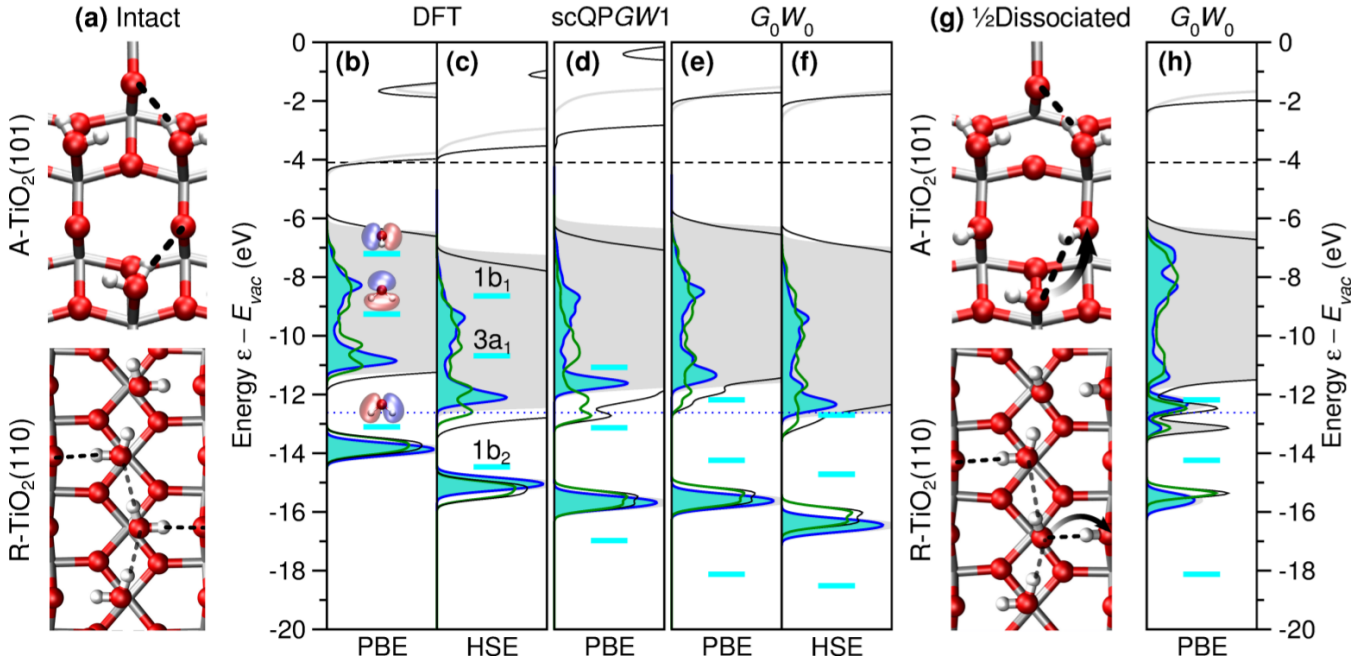


Figure 3. (a-f) IML intact and (g,h) $\frac{1}{2}$ dissociated H_2O adsorbed on coordinately unsaturated Ti sites ($\text{H}_2\text{O}@Ti_{cus}$). A- $\text{TiO}_2(101)$ /R- $\text{TiO}_2(110)$ ²¹ total (grey/black) and H_2O projected (blue/green) DOS computed with (b,c) DFT, (d) scQPGW1, and (e,f,h) G_0W_0 using the (b,d,e,h) generalized gradient approximation (PBE)³⁷ and (c,f) range-separated hybrid (HSE)³⁹ for the xc-functional. Filling denotes occupation for A- $\text{TiO}_2(101)$. Energies are relative to the vacuum level, E_{vac} . The measured ϵ_{CBM} ⁴¹ (black dashed line), measured and coupled-cluster (CCSD(T)) H_2O gas phase ionization potentials IP ⁷¹ (blue dotted line), and for each level of theory the calculated gas phase $1b_1$, $3a_1$, and $1b_2$ H_2O levels²¹ (marked in cyan) are provided. Note that the fully symmetric $2a_1$ H_2O levels lie below -20 eV. (a,g) Charge transfer of about $-0.4e$ accompanying deprotonation is represented by arrows, while intermolecular (gray) and interfacial (black) hydrogen bonds are denoted by dotted lines. Ti, O, and H atoms are depicted in silver, red, and white, respectively.

tive ordering is also consistent with that obtained from KS eigenvalues using the B3LYP xc-functional of 8.24⁷⁴ and 8.6 eV⁷⁵ for A- $\text{TiO}_2(101)$ and R- $\text{TiO}_2(110)$, respectively. This qualitative agreement provides further support for the reliability of our G_0W_0 approach.

3.2. H_2O Intact and $\frac{1}{2}$ Dissociated on Coordinately Unsaturated Ti Sites. For coverages up to 1ML, H_2O adsorbs molecularly on the A- $\text{TiO}_2(101)$ surface, with O bonding to Ti_{cus} and one H forming an interfacial hydrogen bond with O_{br} ,^{8,11,76–78} as shown in Figure 3(a). On R- $\text{TiO}_2(110)$, the distance between the nearest neighboring Ti_{cus} sites is shorter, allowing additional intermolecular hydrogen bonds to form along the [001] direction,^{79–82} as show in Figure 3(a).

The QP level alignment relative to the vacuum level E_{vac} for 1ML of H_2O adsorbed intact on A- $\text{TiO}_2(101)$ and R- $\text{TiO}_2(110)$ ²¹ are shown in Figure 3(b-f). These are compared to the $1b_2$, $3a_1$, and $1b_1$ levels’ absolute alignment for gas phase H_2O .²¹ Specifically, we analyze the dependence of the H_2O PDOS on the methodology: PBE DFT, HSE DFT, PBE scQPGW1, PBE G_0W_0 , and HSE G_0W_0 .

As was previously found for the H_2O -R- $\text{TiO}_2(110)$ interface, the IP for H_2O -A- $\text{TiO}_2(101)$ is ordered according to the method’s description of the screening, ϵ_{∞}^{-1} .²¹ As shown in Table 3, the IP is ordered as PBE G_0W_0 (6.3 eV) \approx PBE scQPGW1 (6.3 eV) \sim PBE DFT (6.4 eV) $<$ HSE G_0W_0 (6.9 eV) $<$ HSE DFT (7.2 eV).

Note that the CBM and VBM relative to E_{vac} from PBE scQPGW1 and PBE G_0W_0 are essentially the same for H_2O -A- $\text{TiO}_2(101)$, but are significantly lower for H_2O -R- $\text{TiO}_2(110)$. This is because the dielectric constant employed in both single-shot PBE scQPGW1 and PBE G_0W_0 are those obtained from PBE DFT, whereas when the QP self energies are “mixed” with the DFT xc-potential in each cycle, as for H_2O -R- $\text{TiO}_2(110)$, the scQPGW1 dielectric constant is significantly reduced relative to PBE DFT. This demonstrates that without mixing of the self energy, for the QP

Table 3. Ionization Potentials IP in eV of 1ML $\text{H}_2\text{O}@Ti_{cus}$ on A- $\text{TiO}_2(101)$ and R- $\text{TiO}_2(110)$.

method	xc-functional	$\text{H}_2\text{O}@Ti_{cus}$	
		A- $\text{TiO}_2(101)$	R- $\text{TiO}_2(110)$
DFT	PBE	6.4	6.2 ^a
	HSE	7.2	7.3 ^a
scQPGW1	PBE	6.3	6.6 ^a
	PBE	6.3	6.0 ^a
G_0W_0	HSE	6.9	6.5 ^a

^aRef. 21

PDOS the PBE scQPGW1 procedure provides no advantage over PBE G_0W_0 , as predicted in ref. 21.

Generally, the highest H_2O PDOS peaks, ϵ_{peak}^{PDOS} , follow the same ordering as the IP s. This suggests that ϵ_{peak}^{PDOS} is pinned to the VBM of the H_2O -A- $\text{TiO}_2(101)$ interface. This is also the case for 1ML intact $\text{H}_2\text{O}@Ti_{cus}$ on R- $\text{TiO}_2(110)$.²¹ However, this ordering of the IP s is completely different from that found for gas phase H_2O .²¹ In this case, the IP is the energy needed to remove one electron from the H_2O $1b_1$ level. Here, the IP s increase with decreasing screening within the methodology until $\epsilon_{\infty} \sim 1$.²¹

However, for 1ML intact $\text{H}_2\text{O}@Ti_{cus}$, the relative alignment of the A- $\text{TiO}_2(101)$ and R- $\text{TiO}_2(110)$ VBMs differs qualitatively with methodology. The IP s obtained from PBE DFT and PBE G_0W_0 are higher (~ 0.2 and 0.3 eV) for A- $\text{TiO}_2(101)$ than for R- $\text{TiO}_2(110)$. However, the IP from HSE DFT is lower (~ -0.1 eV) for A- $\text{TiO}_2(101)$ than R- $\text{TiO}_2(110)$, while the opposite is true for HSE G_0W_0 (~ 0.4 eV). Thus, independently of the xc-functional employed, G_0W_0 yields higher IP s for 1ML intact $\text{H}_2\text{O}@Ti_{cus}$ on A- $\text{TiO}_2(101)$ than on R- $\text{TiO}_2(110)$. This is contrary to our findings for the clean A- $\text{TiO}_2(101)$ and R- $\text{TiO}_2(110)$ surface, and sug-

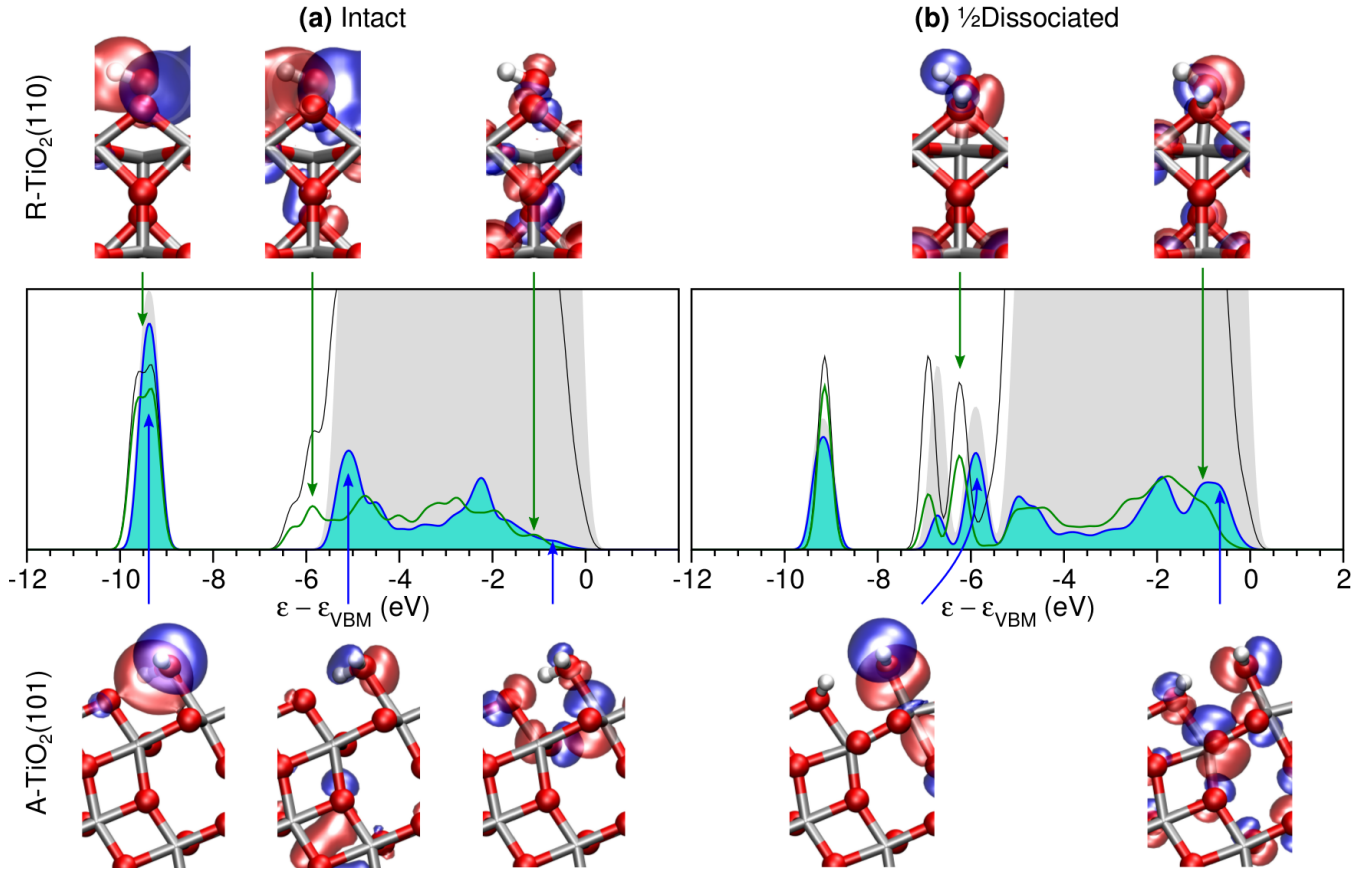


Figure 4. (a) IML intact and (b) $\frac{1}{2}$ dissociated H_2O adsorbed on coordinately unsaturated Ti sites ($\text{H}_2\text{O}@T_{icus}$). Total (grey/black) and H_2O projected (blue/green) G_0W_0 DOS on anatase $\text{TiO}_2(101)$ /rutile $\text{TiO}_2(110)$ surfaces and selected orbitals are shown schematically below/above. Energies are relative to the valence band maximum, ϵ_{VBM} . Ti, O, and H atoms are depicted in silver, red, and white, respectively.

gests that H_2O adsorption inverts the relative positions of the A- $\text{TiO}_2(101)$ and R- $\text{TiO}_2(110)$ VBMs.

Although we find the position of the lower edge of the valence band is only weakly affected by adsorbing H_2O on either A- $\text{TiO}_2(101)$ or R- $\text{TiO}_2(110)$, the VBM is shifted up by about 1 eV in both cases. This is consistent with the experimentally observed change in work function for the liquid water–R- $\text{TiO}_2(110)$ interface.^{21,26,41–45,83}

The reordering of the HSE DFT and G_0W_0 IPs for 1ML intact H_2O on A- $\text{TiO}_2(101)$ and R- $\text{TiO}_2(110)$ may be attributed to the greater difference between the constant screening built into HSE DFT⁴⁷ and the screening of rutile compared to anatase. Essentially, the fraction of the Hartree-Fock exact-exchange which is incorporated within HSE, $\alpha = 0.25$, acts as an effective inverse dielectric constant within the system, $\alpha \sim \epsilon_\infty^{-1}$.⁴⁷ As a result, for materials with $\epsilon_\infty \approx 4$, HSE DFT and G_0W_0 should provide similar descriptions of the screening.⁴⁷ From Table 2, we see that the RPA, BSE, and measured ϵ_∞ agree qualitatively and are consistently lower and closer to the HSE DFT effective dielectric constant of $\epsilon_\infty \sim 4$ for A- TiO_2 compared to R- TiO_2 . For this reason, as shown in Figure 3, the difference between HSE DFT and G_0W_0 IPs is larger for R- TiO_2 than A- TiO_2 , resulting in their relative reordering at the G_0W_0 level. This demonstrates the important role played by the screening in describing the relative alignment of anatase and rutile polymorphs.

Overall the H_2O QP PDOS for 1ML intact $\text{H}_2\text{O}@T_{icus}$ is similar for the A- $\text{TiO}_2(101)$ and R- $\text{TiO}_2(110)$ surfaces. In particular, the most strongly bound $1b_2$ peaks and the upper edges of the H_2O PDOS spectra have similar energies for the two polymorphs over

all five levels of theory (*cf.* Figure 3(b-f)).

On A- $\text{TiO}_2(101)$, the IML intact H_2O QP PDOS generally consists of three distinct peaks, which have clear contributions from molecular $1b_2$, $3a_1$ and $1b_1$ levels (*cf.* Figure 3(b) and Figure 4(a)). This is in contrast to R- $\text{TiO}_2(110)$, where the H_2O QP PDOS consists of many more peaks, with a greater hybridization at IML compared to $\frac{1}{2}$ ML coverage on the R- $\text{TiO}_2(110)$ substrate.²¹ This may be attributed to stronger intermolecular interactions on R- $\text{TiO}_2(110)$ due to its shorter T_{icus} nearest neighbor separations ($d[T_{icus} - T_{icus}] \approx 2.96 \text{ \AA}$) versus A- $\text{TiO}_2(101)$ ($d[T_{icus} - T_{icus}] \approx 3.78 \text{ \AA}$). This leads to intermolecular bonding and antibonding levels, which may further hybridize with the substrate.²¹ For example, as shown in Figure 3, the bottom edge of the $3a_1$ peak for A- $\text{TiO}_2(101)$ is higher than that of R- $\text{TiO}_2(110)$. This is because on R- $\text{TiO}_2(110)$ the $3a_1$ levels of neighbouring molecules hybridize to form intermolecular bonding and antibonding combinations.²¹ These give rise to separate peaks below and above the bottom edge of the R- $\text{TiO}_2(110)$ valence band. As a result, the QP H_2O PDOS for 1ML intact $\text{H}_2\text{O}@T_{icus}$ on R- $\text{TiO}_2(110)$ has the $3a_1$ intermolecular bonding level below the bottom of the valence band, while for A- $\text{TiO}_2(101)$, the $3a_1$ level is completely within the substrate’s valence band.

Figure 3(g) shows the structures of $\frac{1}{2}$ dissociated $\text{H}_2\text{O}@T_{icus}$ on A- $\text{TiO}_2(101)$ and R- $\text{TiO}_2(110)$. In both cases, one proton from $\text{H}_2\text{O}@T_{icus}$ is transferred to the adjacent O_{br} . This results in two distinct OH groups: $\text{HO}@T_{icus}$ and $O_{br}\text{H}$. This process is accompanied by a $-0.4e$ charge transfer from $\text{HO}@T_{icus}$ to $O_{br}\text{H}$, as depicted schematically in Figure 3(g).

Although the resulting PBE G_0W_0 QP DOS shown in Figure 3(e)

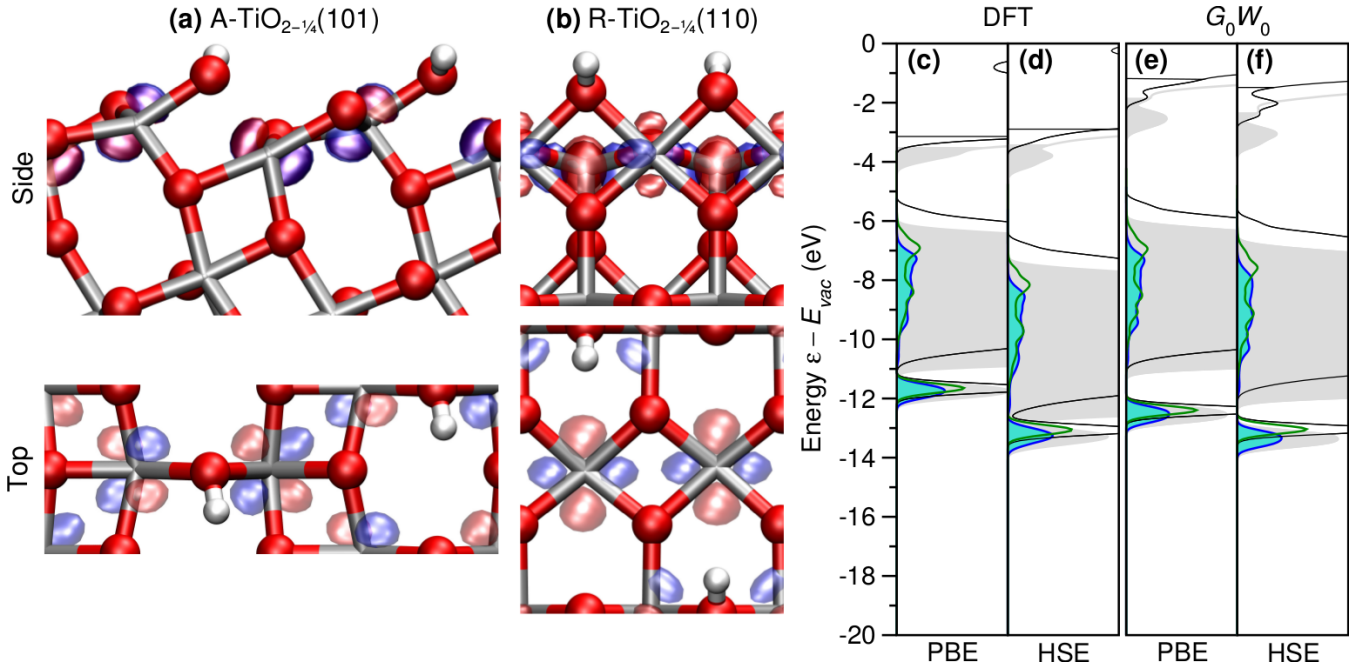


Figure 5. $\frac{1}{2}$ ML H_2O dissociated on bridging O vacancies ($\text{H}_2\text{O}@O_{br}^{vac}$) of defective (a,b) $\text{A-TiO}_{2-\frac{1}{4}}(101)/\text{R-TiO}_{2-\frac{1}{4}}(110)$ ²¹ surfaces with $\frac{1}{2}$ ML of O_{br}^{vac} . Total (grey/black) and H_2O projected (blue/green) DOS computed with (c,d) DFT and (e,f) G_0W_0 using the (c,e) generalized gradient approximation (PBE)³⁷ and (d,f) range-separated hybrid (HSE)³⁹ for the xc-functional. Filling denotes occupation for $\text{A-TiO}_{2-\frac{1}{4}}(101)$. Horizontal black lines denote Fermi levels ϵ_F for $\text{R-TiO}_{2-\frac{1}{4}}(110)$. Energies are relative to the vacuum level, E_{vac} . Ti, O, and H atoms are depicted in silver, red, and white, respectively.

and (h) are generally similar, there are important differences which are related to the $\text{H}_2\text{O}@Ti_{cus}$ dissociation. For the dissociated H_2O molecule, the $1b_2$ peak is replaced by separate $\text{HO}@Ti_{cus}$ and $O_{br}H$ peaks at about -12.5 and -13 eV below E_{vac} (see Figure 3(h)), with O-H σ character on both $\text{A-TiO}_2(101)$ and $\text{R-TiO}_2(110)$ ²¹ (see Figure 4(b)). These peaks are at such similar energies on both $\text{A-TiO}_2(101)$ and $\text{R-TiO}_2(110)$ because they are well separated from the bottom edge of the TiO_2 valence band.

As mentioned above, the three distinct peaks in the H_2O PDOS on both $\text{A-TiO}_2(101)$ and $\text{R-TiO}_2(110)$ are associated with the $1b_2$, $3a_1$, and $1b_1$ gas phase H_2O levels. This is clearly seen by comparing the molecular components of the orbitals depicted for 1ML intact and $\frac{1}{2}$ dissociated $\text{H}_2\text{O}@Ti_{cus}$ on both $\text{A-TiO}_2(101)$ and $\text{R-TiO}_2(110)$ in Figure 4 with the gas phase H_2O levels depicted in Figure 3. There is significantly greater hybridization between the molecular levels on $\text{R-TiO}_2(110)$ compared to $\text{A-TiO}_2(101)$. Specifically, on $\text{R-TiO}_2(110)$ there are obvious bonding and antibonding combinations of the $1b_2$ levels and $3a_1$ levels between neighbouring H_2O molecules.²¹ Such intermolecular hybridization does not occur for $\text{A-TiO}_2(101)$, as the molecules are too far apart.

More importantly, ϵ_{peak}^{PDOS} is shifted to higher energy upon dissociation, with a greater shift for $\text{A-TiO}_2(101)$ versus $\text{R-TiO}_2(110)$. To explain these differences, and their potential impact on the interfaces' photocatalytic activity, one should compare the level alignment relative to the VBM. In so doing, one can directly compare the relative propensity for photogenerated hole transfer from the substrate's VBM to the molecular HOMO for $\text{A-TiO}_2(101)$ and $\text{R-TiO}_2(110)$.

In Figure 4 we provide the level alignment relative to the VBM for (a) intact and (b) $\frac{1}{2}$ dissociated H_2O on $\text{A-TiO}_2(101)$ and $\text{R-TiO}_2(110)$. The level alignment shown in Figure 4 suggests that (1) hole trapping is more favored on $\text{A-TiO}_2(101)$ than $\text{R-TiO}_2(110)$ and (2) $\text{HO}@Ti_{cus}$ is more photocatalytically active than intact $\text{H}_2\text{O}@Ti_{cus}$. This is based on the following observations: (1) ϵ_{peak}^{PDOS} is about 0.5 eV higher in energy for $\text{A-TiO}_2(101)$

than $\text{R-TiO}_2(110)$; (2) ϵ_{peak}^{PDOS} is about 0.1 eV closer to the VBM for $\text{HO}@Ti_{cus}$ than for intact $\text{H}_2\text{O}@Ti_{cus}$; (3) the PDOS for $\text{HO}@Ti_{cus}$ at ϵ_{peak}^{PDOS} is an order of magnitude greater than for intact $\text{H}_2\text{O}@Ti_{cus}$; and (4) the HOMO is more localized on the molecule for $\text{HO}@Ti_{cus}$ than for intact $\text{H}_2\text{O}@Ti_{cus}$.

These conclusions are reinforced by analyzing the HOMOs at Γ shown in Figure 4. Here, one clearly sees that the HOMOs have greater weight on the molecule for $\text{HO}@Ti_{cus}$ than intact $\text{H}_2\text{O}@Ti_{cus}$. This should promote hole trapping on $\text{HO}@Ti_{cus}$. Although there is only a small (0.1 eV) energy difference between the HOMO for $\frac{1}{2}$ dissociated and intact $\text{H}_2\text{O}@Ti_{cus}$, the latter level is not photocatalytically relevant for hole trapping on the molecule. This is because it is a lone-pair orbital that datively bonds to Ti_{cus} . For this reason, if an electron were extracted from this level, one would instead expect the hole to remain on the surface, and H_2O to desorb from Ti_{cus} . This agrees with previous studies of the liquid $\text{H}_2\text{O}-\text{A-TiO}_2(101)$ interface, which found that localizing the hole on intact H_2O is inherently unstable, and leads to deprotonation.¹⁷ Instead, the hole localizes on 3-fold coordinated surface O (O_{3fold}) atoms.¹⁷

In contrast to the intact $\text{H}_2\text{O}@Ti_{cus}$ HOMOs, the HOMOs for $\text{HO}@Ti_{cus}$ on $\text{A-TiO}_2(101)$ and $\text{R-TiO}_2(110)$ are the photocatalytically active levels for hole-trapping. Indeed, they have the same character as the hole trapping levels reported in the literature for $\text{A-TiO}_2(101)$ ¹⁷ and $\text{R-TiO}_2(110)$.²² In particular, they have both $O_{3fold} 2p\pi$ ⁸⁴ and OH 2p character. While in the case of $\text{HO}@Ti_{cus}$, this orbital is doubly occupied, in the trapped hole structures of refs. 17 and 22, the OH groups are bent towards the surface, with the hole shared between $O_{3fold} 2p\pi$ and OH 2p orbitals.

This clearly demonstrates that a HOMO initially below the VBM can, upon light absorption and subsequent nuclear relaxation, evolve into a hole trapping level of the interface. This justifies our use of ground state level alignment for comparing photocatalytic activity among $\text{H}_2\text{O}-\text{TiO}_2$ interfaces.

Although hole trapping has been documented for both A-

TiO₂(101)¹⁷ and R-TiO₂(110),^{22,85} the more favorable ground state HOMO level alignment for A-TiO₂(101) may explain why the anatase polymorph shows higher photocatalytic activity than the rutile polymorph.^{15,86,87}

3.3. H₂O Dissociated on Bridging O Vacancies. For R-TiO₂(110), the most stable O vacancies are at surface O_{br} sites, i.e., O_{br}^{vac}. These sites mediate H₂O dissociation on R-TiO₂(110),^{31,88} For A-TiO₂(101), the most stable O vacancies are subsurface.^{6,89} However, after H₂O adsorption, these subsurface vacancies migrate to the surface and are filled by H₂O, i.e., H₂O@O_{br}^{vac}, which subsequently dissociates to form 2HO_{br}.^{89,90} This results in a structure equivalent to H on a stoichiometric A-TiO₂(101) surface.^{89–91} For this reason, we consider a ½ML coverage of H₂O adsorbed dissociatively on O_{br}^{vac} sites (H₂O@O_{br}^{vac}) of a defective A-TiO_{2–¼}(101) or R-TiO_{2–¼}(110)²¹ surface consisting of ½ML of O_{br}^{vac}, shown schematically in Figure 5. This is equivalent to 1ML of H adsorbed on O_{br} (H@O_{br}) of a stoichiometric A-TiO₂(101) or R-TiO₂(110) surface.

These hydroxylated structures have occupied Ti 3d levels which are associated with reduced Ti³⁺ atoms. The excess electrons introduce *n*-type doping. These occupied Ti³⁺ 3d levels give rise to the charge density just below the Fermi level, ε_F, in the DOS shown in Figure 5(c-f).⁸³

The difference in spatial and energetic localization of the Ti³⁺ 3d levels between O defective A-TiO₂(101) and R-TiO₂(110) has been recently probed via STM.⁹² For O_{br}^{vac}@A-TiO₂(101) at 6 K, the excess electrons are strictly localized next to O_{br}^{vac},⁹² while for O_{br}^{vac}@R-TiO₂(110) at 78 K, the excess electrons are not confined next to O_{br}^{vac}.^{92,93} Instead, the excess electrons in O_{br}^{vac}@R-TiO₂(110) may occupy 3d levels of surface Ti_{cus} or subsurface Ti atoms.

We find for ½ML H₂O@O_{br}^{vac} on both A-TiO_{2–¼}(101) and R-TiO_{2–¼}(110), the highest energy occupied Ti³⁺ 3d levels⁸⁴ are mostly on surface Ti atoms, as shown in Figure 5(a,b). These predominantly Ti 3d_{x²–y²} levels⁸⁴ are bonding along the [010] and [001] directions for A-TiO_{2–¼}(101) and R-TiO_{2–¼}(110), respectively. Furthermore, for H₂O@O_{br}^{vac} on A-TiO_{2–¼}(101), the level occupies HO_{br}'s nearest neighbor Ti atoms. For H₂O@O_{br}^{vac} on R-TiO_{2–¼}(110), this level also has weight on the next next nearest neighbour Ti_{cus} atoms. Additionally, there are higher energy occupied Ti 3d levels on subsurface Ti atoms.

In PBE DFT, the occupied Ti 3d levels form a shoulder at the bottom edge of the conduction band for H₂O@O_{br}^{vac} on A-TiO_{2–¼}(101), whereas on R-TiO_{2–¼}(110) they do not even form a shoulder, as shown in Figure 5(c). The degree of energetic localization of the Ti³⁺ 3d levels, and their energy ε_{Ti³⁺} below ε_F, increases with the level of theory from PBE DFT < HSE DFT (ε_{Ti³⁺} ~ 0.6, 0.4 eV) < PBE G₀W₀ (ε_{Ti³⁺} ~ 0.7, 0.6 eV) < HSE G₀W₀ (ε_{Ti³⁺} ~ 1.0, 0.9 eV) for H₂O@O_{br}^{vac} on A-TiO_{2–¼}(101)/R-TiO_{2–¼}(110), and is generally higher (0.1 eV) for A-TiO_{2–¼}(101) than R-TiO_{2–¼}(110), as shown in Table 4. This is consistent with the ε_{Ti³⁺} ~ 1 eV measured for O defective A-TiO₂(101) and R-TiO₂(110) and HO_{br}@R-TiO₂(110) by scanning tunneling spectroscopy (STS),^{92–94} photoemission electron spectroscopy (PES),^{32,95} and two photon photoemission spectroscopy (2PP).^{83,96} However, a full treatment of Ti 3d defect levels, e.g., due to interstitial Ti atoms, also requires the inclusion of electron-phonon interactions.^{93,97}

Overall, relative to E_{vac}, the levels of A-TiO_{2–¼}(101) are consistently about 0.6 eV lower in energy than those of R-TiO_{2–¼}(110), for PBE DFT, HSE DFT, PBE G₀W₀, and HSE G₀W₀, as shown in Figure 5(c-f). However, the H₂O@O_{br}^{vac} 1b₂ levels are at similar energies (within 0.2 eV) on A-TiO_{2–¼}(101) and R-TiO_{2–¼}(110),

Table 4. Occupied Ti³⁺ 3d Level Energies ε_{Ti³⁺} in eV Below the Fermi Level ε_F for ½ML Dissociated H₂O@O_{br}^{vac} on A-TiO_{2–¼}(101) and R-TiO_{2–¼}(110).

method	xc-functional	H ₂ O@O _{br} ^{vac}	
		A-TiO _{2–¼} (101)	R-TiO _{2–¼} (110)
DFT	PBE	0.2	0.1 ^a
	HSE	0.6	0.4 ^a
G ₀ W ₀	PBE	0.7	0.6 ^a
	HSE	1.0	0.9 ^a
STS		1.0 ± 0.1 ^b	0.7 ± 0.1 ^b
			0.9 ^c
PES		1.1 ^d	0.9 ^d
			0.8 ^e
2PP			0.9 ^g
			0.9 ^g

^aRef. 21. ^bRef. 92. ^cRef. 93. ^dRef. 95. ^eRef. 32. ^fRefs. 83 and 96.

for PBE DFT, HSE DFT, PBE G₀W₀, and HSE G₀W₀, as shown in Figure 5(c-f).

Focusing on the *IP* from PBE G₀W₀ shown in Table 5, they are ordered: R-TiO₂(110) (7.29 eV) ≈ A-TiO₂(101) (7.15 eV) > H₂O@Ti_{cus} on A-TiO₂(101) (6.25 eV) ≈ H₂O@O_{br}^{vac} on A-TiO_{2–¼}(101) (6.19 eV) ≈ H₂O@Ti_{cus} on R-TiO₂(110) (6.03 eV) > H₂O@O_{br}^{vac} on A-TiO_{2–¼}(101) (5.37 eV). On the one hand, there are no significant differences in *IP* between bare and H₂O@Ti_{cus} covered A-TiO₂(101) and R-TiO₂(110). On the other hand, for H₂O dissociatively adsorbed on O_{br}^{vac} sites of defective A-TiO_{2–¼}(101) and R-TiO_{2–¼}(110), the *IP*s are significantly different, despite having quite similar HO_{br} concentrations per unit area. The origin of this difference might be related to differences in the structure's relative stability or surface dipole.⁸²

Table 5. Ionization Potentials *IP* in eV from PBE G₀W₀ for A-TiO₂(101) and R-TiO₂(110)

coverage	surface	<i>IP</i> (eV)
clean	A-TiO ₂ (101)	7.15
	R-TiO ₂ (110)	7.29 ^a
1ML H ₂ O@Ti _{cus}	A-TiO ₂ (101)	6.25
	R-TiO ₂ (110)	6.03 ^b
1ML H ₂ O@O _{br} ^{vac}	A-TiO _{2–¼} (101)	6.19
	R-TiO _{2–¼} (110)	5.37 ^b

^aRef. 26. ^bRef. 21.

Similarly, ε_{peak}^{PDOS} for dissociatively adsorbed H₂O@O_{br}^{vac} on A-TiO_{2–¼}(101) is about 0.4 eV below that on R-TiO_{2–¼}(110). Since ε_{peak}^{PDOS} is thus closer to the standard hydrogen electrode (SHE) for H₂O@O_{br}^{vac} on R-TiO_{2–¼}(110) than A-TiO_{2–¼}(101), one would expect the former structure to require a smaller overpotential and be more active than the latter within an electrochemical cell.⁹⁸ However, for photocatalysis, the alignment of ε_{peak}^{PDOS} relative to ε_{VBM} is the more relevant quantity. As we shall see in the next section, the relative electrochemical and photocatalytic activities of these two structures are reversed.

3.4. Coverage and Dissociation Dependence of H₂O Spectra for Stoichiometric and Defective Surfaces. To systematically investigate the similarities and differences between A-TiO₂(101) and R-TiO₂(110) surfaces, we consider a variety of coverages of intact and dissociated H₂O on stoichiometric A-TiO₂(101) [Figure 6(a)] and defective A-TiO_{2–¼}(101) [Figure 6(b,c)], as done previously for the rutile surface.²¹ These configurations are consistent with previous results for H₂O on A-TiO₂.^{8,11,76–78,90,99–102}

The adsorption energies shown in Table 6 and Figure 7(a,b) for

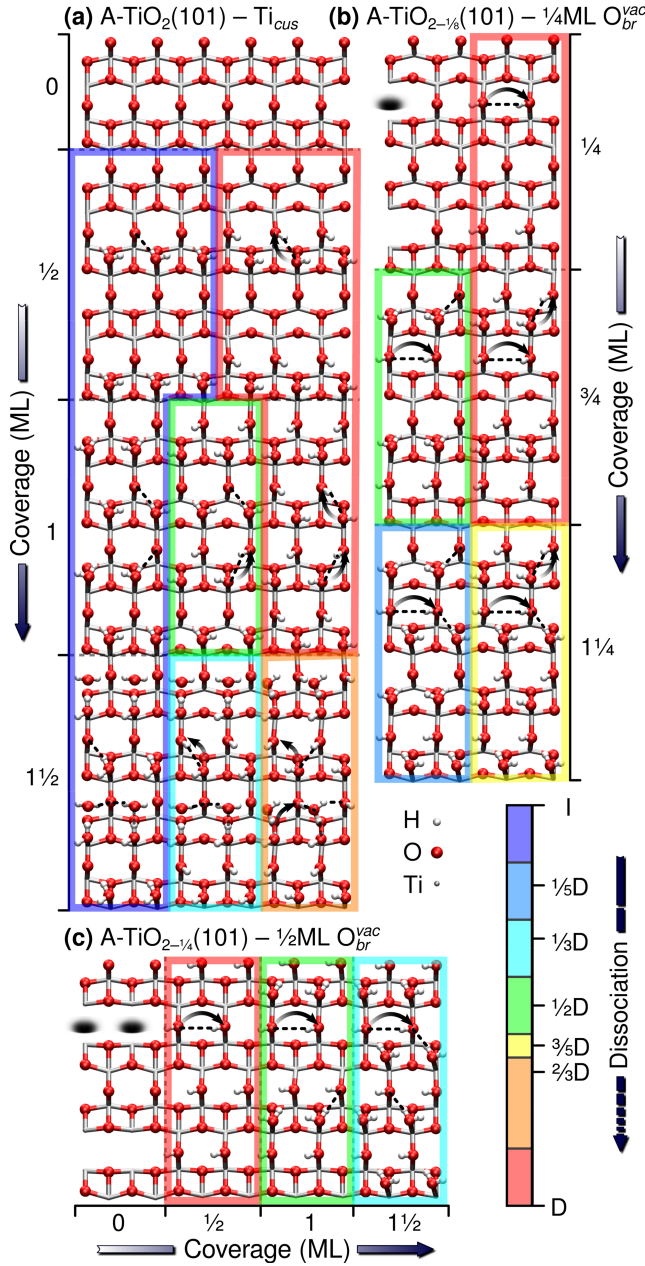


Figure 6. Schematics of H₂O adsorbed intact (I) or dissociated (D) on (a) coordinately unsaturated Ti sites (Ti_{cus}) of stoichiometric A-TiO₂(101) and (b) $\frac{1}{4}$ ML or (c) $\frac{1}{2}$ ML of bridging O vacancies (O_{br}^{vac}) on defective A-TiO_{2-x}(101), where $x = \frac{1}{8}$ and $\frac{1}{4}$, respectively. Coverage is half the number of H₂O formula units per (101) 1×1 unit area of the clean stoichiometric or defective surface. Dissociation is the fraction of H₂O molecules which are dissociated. Charge transfer of about $-0.4e$ accompanying deprotonation is represented by arrows, while intermolecular (gray) and interfacial (black) hydrogen bonds are denoted by dotted lines.

H₂O on A-TiO₂, A-TiO_{2-1/8}, and A-TiO_{2-1/4} (101) are generally similar to those on R-TiO₂, R-TiO_{2-1/8}, and R-TiO_{2-1/4} (110),²¹ respectively. On both A-TiO₂(101) and R-TiO₂(110), intact H₂O adsorption is more stable than dissociative adsorption from $\frac{1}{2}$ and $1\frac{1}{2}$ ML coverages. The adsorption energies for H₂O@Ti_{cus} on A-TiO₂(101) follow the same trend as on R-TiO₂(110), but are somewhat stronger on A-TiO₂(101), with the greatest differences seen for dissociatively adsorbed H₂O. Since the photocatalytically active species HO_{br}@Ti_{cus} is more stable on A-TiO₂(101) than R-TiO₂(110), this also suggests that A-TiO₂(101) should be more photocatalytically active than R-TiO₂(110). This is because one

Table 6. Adsorption Energies E_{ads} , Highest PDOS Peaks ϵ_{peak}^{PDOS} and Average PDOS HOMO Energies ϵ_{HOMO}^{PDOS} in eV of H₂O on Ti_{cus} of Stoichiometric A-TiO₂(101) and R-TiO₂(110) and O_{br}^{vac} of Defective A-TiO_{2-x}(101) and R-TiO_{2-x}(110) with $x = \frac{1}{8}$ or $\frac{1}{4}$.

coverage		A-TiO _{2-x} (101)			R-TiO _{2-x} (110)		
ML	x	E_{ads}	ϵ_{HOMO}^{PDOS}	ϵ_{peak}^{PDOS}	E_{ads}	ϵ_{HOMO}^{PDOS}	ϵ_{peak}^{PDOS}
$\frac{1}{2}$	I 0	-0.38	-1.42	-0.7	-0.33	-1.44	-1.2
	D 0	-0.18	-0.49	-0.7	-0.13	-1.03	-0.8
1	I 0	-0.37	-1.07	-0.6	-0.41	-1.28	-1.1 ^a
	D 0	-0.29	-0.43	-0.5	-0.23	-0.79	-1.0 ^a
$1\frac{1}{2}$	I 0	-0.35	-0.72	-0.7	-0.34	-0.99	-1.3
	D 0	-0.26	-0.45	-0.5	-0.10	-0.68	-0.9 ^a
$\frac{1}{4}$	$\frac{1}{8}$ D 0	-0.27	-0.42	-0.7	-0.17	-0.68	-1.1
	$\frac{3}{8}$ D 0	-0.24	-0.39	-0.8	-0.12	-0.65	-0.9
$\frac{3}{4}$	$\frac{1}{8}$ D $\frac{1}{8}$	-1.35	-1.27	-1.0	-0.83	-1.37	-1.1
	$\frac{3}{8}$ D $\frac{3}{8}$	-0.69	-1.04	-0.8	-0.44	-1.15	-1.1
$1\frac{1}{4}$	$\frac{1}{8}$ D $\frac{1}{8}$	-0.60	-0.58	-0.7	-0.34	-0.79	-0.8
	$\frac{3}{8}$ D $\frac{3}{8}$	-0.50	-1.00	-0.6	-0.47	-1.15	-1.0
$1\frac{1}{2}$	$\frac{1}{8}$ D $\frac{1}{8}$	-0.43	-0.53	-0.6	-0.40	-0.75	-1.0
	D $\frac{1}{4}$	-1.35	-0.92	-0.6	-1.32	-1.18	-1.1 ^a
1	$\frac{1}{2}$ D $\frac{1}{4}$	-0.68	-0.90	-0.6	-0.77	-1.12	-1.1
$1\frac{1}{2}$	$\frac{1}{3}$ D $\frac{1}{4}$	-0.55	-0.99	-0.6	-0.69	-1.22	-1.0

^aRef. 21.

expects there to be more HO_{br}@Ti_{cus} on A-TiO₂(101) than R-TiO₂(110).

On the defective surfaces, intact H₂O adsorption is also more stable than dissociative adsorption on A-TiO_{2-1/8}(101)/R-TiO_{2-1/8}(110) and A-TiO_{2-1/4}(101)/R-TiO_{2-1/4}(110). Dissociative H₂O@O_{br}^{vac} adsorption is generally stronger on A-TiO_{2-1/4}(101)/A-TiO_{2-1/8}(101) than R-TiO_{2-1/4}(110)/R-TiO_{2-1/8}(110) surfaces, except for $1\frac{1}{2}$ ML $\frac{1}{8}$ D H₂O@O_{br}^{vac}.

However, the adsorption energies shown in Figure 7(b) are strongly dependent on the stability of the defective A-TiO_{2-1/4}(101)/R-TiO_{2-1/4}(110) and A-TiO_{2-1/8}(101)/R-TiO_{2-1/8}(110) structures with surface O_{br}^{vac}. Since surface O_{br}^{vac} are less stable than subsurface O vacancies for A-TiO₂(101), the adsorption energies on A-TiO_{2-x}(101) provided in Figure 7(b) are somewhat overestimated.

Figure 7(c,d) shows the PBE G_0W_0 H₂O PDOS relative to ϵ_{VBM} as a function of coverage and dissociation for the structures shown in Figure 6. Overall the PDOS on A-TiO₂(101) and R-TiO₂(110) are in surprisingly close agreement, both in shape and energy. For $\frac{1}{2}$ ML of H₂O, peaks related to the H₂O 1b₂, 3a₁ and 1b₁ levels (cf. Figure 3(b)) are clearly evident. When the coverage is increased to more than 1ML, there are larger differences between the H₂O PDOS on A-TiO₂(101) and R-TiO₂(110). This may be attributed to the different intermolecular and interfacial interactions induced by the different hydrogen bonding networks. For $1\frac{1}{2}$ ML H₂O on A-TiO₂(101), the peak associated with the H₂O 1b₂ level, which is located at -8 eV, is more delocalized than rutile. This is because there are more interfacial interactions between H₂O and A-TiO₂(101). For $1\frac{1}{4}$ ML H₂O on O_{br}^{vac} ($\frac{1}{8}$ D), the water 1b₂ level splits into two peaks, as H₂O and HO_{br} form two lines of hydrogen bonding networks. We also find the bottom of the valance band for H₂O on A-TiO₂, A-TiO_{2-1/8}, and A-TiO_{2-1/4} (101) is higher than that of R-TiO₂, R-TiO_{2-1/8}, and R-TiO_{2-1/4} (110). This is attributable to the higher VBM of the clean A-TiO₂(101) surface, as depicted by the gray regions in Figure 7.

For all spectra shown in Figure 7(c,d), ϵ_{HOMO}^{PDOS} is higher on A-TiO₂, A-TiO_{2-1/8}, and A-TiO_{2-1/4} (101) than R-TiO₂, R-TiO_{2-1/8},

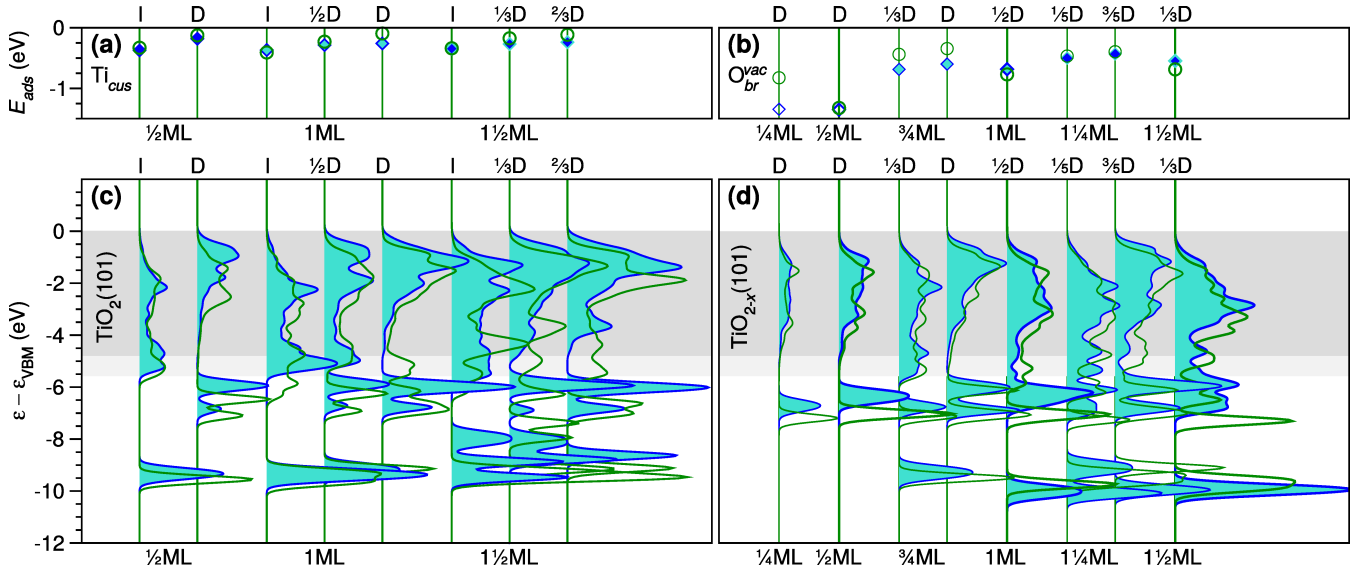


Figure 7. Structure and coverage dependence of (a,b) adsorption energy E_{ads} and (c,d) G_0W_0 PDOS for H_2O adsorbed intact (I) or dissociated (D) on (a,c) coordinately unsaturated Ti sites (Ti_{cus}) of stoichiometric A- $TiO_2(101)$ (blue, Figure 6(a)) and R- $TiO_2(110)^{21}$ (green) and (b,d) bridging O vacancies (O_{br}^{vac}) of defective A- $TiO_{2-x}(101)$ (blue) and R- $TiO_{2-x}(110)^{21}$ (green), with $x = 1/8$ (thin lines, Figure 6(b)) or $1/4$ (thick lines, Figure 6(c)). (a,b) RPBE E_{ads} on A- $TiO_{2-x}(101)$ (\diamond) and R- $TiO_{2-x}(110)^{21}$ (\circ) surfaces ($x = 0, 1/8, 1/4$) for (white) low ($1/4$ and $1/2$ ML), (turquoise) medium ($3/4$ and 1ML), and (blue) high ($1/4$ and $1/2$ ML) coverage. (c,d) Energies are relative to the VBM (ϵ_{VBM}). The clean surface DOS of (c) A- $TiO_2(101)$ /R- $TiO_2(110)$ (dark/light gray regions) are shown for comparison.

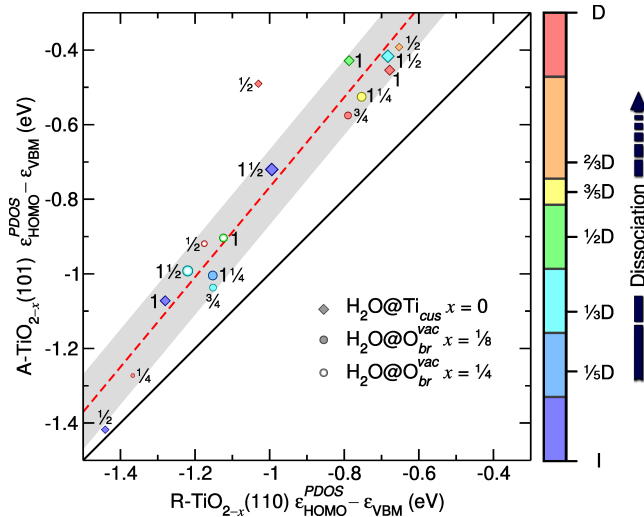


Figure 8. Average energy of G_0W_0 PDOS HOMO ϵ_{HOMO}^{PDOS} in eV of $H_2O@Ti_{cus}$ on stoichiometric A- $TiO_2(101)$ versus R- $TiO_2(110)$ and of $H_2O@O_{br}^{vac}$ on defective A- $TiO_{2-x}(101)$ versus R- $TiO_{2-x}(110)$ for $x = 1/8$ or $1/4$. H_2O total coverage in ML and fraction intact (I) or dissociated (D) are provided. A linear fit (red dashed line) with a standard deviation of ± 0.1 eV (gray regions) is compared to the identity line (black solid line).

and R- $TiO_{2-1/8}(110)$, respectively, as shown in Table 6 and Figure 8. Further, these differences in ϵ_{HOMO}^{PDOS} are larger for dissociated H_2O . Since it is the HOMO of $HO@Ti_{cus}$ which can trap a photo-generated hole, as discussed in section 3.2, the larger differences in ϵ_{HOMO}^{PDOS} shown in Figures 7(c) and 8 for dissociated H_2O suggest A- $TiO_2(101)$ should generally be more photocatalytically active than R- $TiO_2(110)$ from low coverage ($1/2$ ML H_2O) to multi-layered H_2O ($1/2$ ML H_2O).

For $1/2$ ML of dissociatively adsorbed $H_2O@O_{br}^{vac}$, ϵ_{peak}^{PDOS} relative to the VBM for R- $TiO_{2-1/4}(110)$ is below that for A- $TiO_{2-1/4}(101)$. This suggests $HO_{br}@O_{br}^{vac}$ should be more photocatalytically ac-

tive on A- $TiO_{2-1/4}(101)$ compared to R- $TiO_{2-1/4}(110)$. However, as shown in the previous section, the reverse is true for their relative electrochemical activity, i.e., $HO_{br}@O_{br}^{vac}$ on R- $TiO_{2-1/4}(110)$ is expected to be more electrochemically active than A- $TiO_{2-1/4}(101)$. This demonstrates the importance of considering both the absolute level alignment relative to E_{vac} , and the level alignment relative to ϵ_{VBM} .

4. CONCLUSIONS

In heterogeneous catalysis, photocatalytic activity is controlled by the level alignment of the adsorbate and substrate levels. For this reason it is essential to obtain a quantitative description of the interfacial level alignment to determine and predict catalytic activity. This can only be obtained from many-body QP GW calculations, which are necessary to correctly describe the anisotropic screening of electron-electron interactions at the catalyst's interface.

Previously, we have shown that HSE G_0W_0 reliably describes the interfacial level alignment relative to the VBM for highly hybridized and localized molecular levels of H_2O^{21} and CH_3OH^{26} on R- $TiO_2(110)$. Here, we have shown that HSE G_0W_0 also provides a quantitative description of the occupied $Ti^{3+} 3d$ level's alignment relative to the Fermi level on both reduced anatase and rutile polymorphs. These are the levels from which electrons are typically excited in 2PP experiments.^{45,83,96} Since HSE DFT fails in both cases, these results clearly demonstrate the important role played by anisotropic screening of the electron-electron interaction in describing the alignment of these molecular and defect levels.

In this study we have performed an in-depth comparison of the QP GW level alignment for H_2O -A- $TiO_2(101)$ and H_2O -R- $TiO_2(110)$ interfaces for a range of chemically significant structures. We have considered the limits of low and high H_2O coverage, intact to fully dissociated H_2O , and stoichiometric to O defective surface composition. Using the HOMO-VBM level alignment for these systems prior to irradiation ϵ_{HOMO}^{PDOS} , we have established the following trends in their relative photocatalytic activity for H_2O photooxidation. (1) There is a strong linear correlation between

$\epsilon_{\text{HOMO}}^{\text{PDOS}}$ on A-TiO_{2-x}(101) and R-TiO_{2-x}(110). (2) We consistently find H₂O's $\epsilon_{\text{HOMO}}^{\text{PDOS}}$ closer to ϵ_{VBM} for A-TiO₂ than R-TiO₂. (3) These differences in $\epsilon_{\text{HOMO}}^{\text{PDOS}}$ are greater for dissociated H₂O, and increase as $\epsilon_{\text{HOMO}}^{\text{PDOS}}$ approaches ϵ_{VBM} . (4) Overall, $\epsilon_{\text{HOMO}}^{\text{PDOS}}$ approaches ϵ_{VBM} with H₂O dissociation. Altogether, this suggests HO@Ti_{CUS} is more photocatalytically active than intact H₂O@Ti_{CUS} and hole trapping is more favorable on A-TiO₂(101) than R-TiO₂(110). This may explain why the anatase polymorph is generally more photocatalytically active than rutile for H₂O photooxidation.

We have clearly demonstrated that the ground state interfacial level alignment is a key factor in understanding the photocatalytic activity of TiO₂. Moreover, in general, knowledge of an interface's ground state electronic structure can be used to establish trends for predicting photocatalytic activity.

AUTHOR INFORMATION

Corresponding Author

E-mail: duncan.mowbray@gmail.com (D.J.M.)

Notes

The authors declare no competing financial interest.

ACKNOWLEDGMENTS

We acknowledge financial support from the China Scholarship Council (CSC), the European Projects DYNamo (ERC-2010-AdG-267374), CRONOS (280879-2 CRONOS CP-FP7), Cost Actions CM1204 (XLIC), and MP1306 (EuSpec); Spanish Grants (FIS2012-37549-C05-02, FIS2013-46159-C3-1-P, PIB2010US-00652, RYC-2011-09582, JCI-2010-08156); Generalitat de Catalunya (2014SGR301, XRQTC); Grupos Consolidados UPV/EHU del Gobierno Vasco (IT-578-13); NSFC (21003113 and 21121003); MOST (2011CB921404); the Chinese Academy of Sciences President's International Fellowship; and NSF Grant CHE-1213189; and computational time from the Shanghai Supercomputing Center, BSC Red Espanola de Supercomputacion, and EMSL at PNNL by the DOE.

REFERENCES

- Fujishima, A.; Zhang, X.; Tryk, D. A. TiO₂ photocatalysis and related surface phenomena. *Surf. Sci. Rep.* **2008**, *63*, 515–582.
- Diebold, U. The surface science of titanium dioxide. *Surf. Sci. Rep.* **2003**, *48*, 53–229.
- Schneider, J.; Matsuoka, M.; Takeuchi, M.; Zhang, J.; Horiuchi, Y.; Anpo, M.; Bahnemann, D. W. Understanding TiO₂ Photocatalysis: Mechanisms and Materials. *Chem. Rev.* **2014**, *114*, 9919–9986.
- Henderson, M. A. A surface science perspective on TiO₂ photocatalysis. *Surf. Sci. Rep.* **2011**, *66*, 185–297.
- Thompson, T. L.; Yates, J. T. J. Surface Science Studies of the Photoactivation of TiO₂—New Photochemical Processes. *Chem. Rev.* **2006**, *106*, 4428–4453.
- Setvín, M.; Aschauer, U.; Scheiber, P.; Li, Y.-F.; Hou, W.; Schmid, M.; Selloni, A.; Diebold, U. Reaction of O₂ with Subsurface Oxygen Vacancies on TiO₂Anatase (101). *Science* **2013**, *341*, 988–991.
- Henderson, M. A. The interaction of water with solid surfaces: fundamental aspects revisited. *Surf. Sci. Rep.* **2002**, *46*, 1–308.
- Sun, C.; Liu, L.-M.; Selloni, A.; Lu, G. Q. M.; Smith, S. C. Titania-water interactions: a review of theoretical studies. *J. Mater. Chem.* **2010**, *20*, 10319–10334.
- Fujishima, A.; Honda, K. Electrochemical Photolysis of Water at a Semiconductor Electrode. *Nature* **1972**, *238*, 37–38.
- Protti, S.; Albini, A.; Serpone, N. Photocatalytic generation of solar fuels from the reduction of H₂O and CO₂: a look at the patent literature. *Phys. Chem. Chem. Phys.* **2014**, *16*, 19790–19827.
- Vittadini, A.; Selloni, A.; Rotzinger, F. P.; Grätzel, M. Structure and Energetics of Water Adsorbed at TiO₂ Anatase 101 and 001 Surfaces. *Phys. Rev. Lett.* **1998**, *81*, 2954–2957.
- Wang, Y.; Sun, H.; Tan, S.; Feng, H.; Cheng, Z.; Zhao, J.; Zhao, A.; Wang, B.; Luo, Y.; Yang, J.; Hou, J. G. Role of point defects on the reactivity of reconstructed anatase titanium dioxide (001) surface. *Nat. Commun.* **2013**, *4*, 2214.
- Diebold, U.; Ruzsycski, N.; Herman, G.; Selloni, A. One step towards bridging the materials gap: surface studies of TiO₂ anatase. *Catal. Today* **2003**, *85*, 93–100.

- Barnard, A. S.; Curtiss, L. A. Prediction of TiO₂Nanoparticle Phase and Shape Transitions Controlled by Surface Chemistry. *Nano Letters* **2005**, *5*, 1261–1266.
- Kavan, L.; Grätzel, M.; Gilbert, S. E.; Klemenz, C.; Scheel, H. J. Electrochemical and Photoelectrochemical Investigation of Single-Crystal Anatase. *J. Amer. Chem. Soc.* **1996**, *118*, 6716–6723.
- Li, Y.-F.; Liu, Z.-P.; Liu, L.; Gao, W. Mechanism and Activity of Photocatalytic Oxygen Evolution on Titania Anatase in Aqueous Surroundings. *J. Amer. Chem. Soc.* **2010**, *132*, 13008–13015.
- Chen, J.; Li, Y.-F.; Sit, P.; Selloni, A. Chemical Dynamics of the First Proton-Coupled Electron Transfer of Water Oxidation on TiO₂ Anatase. *J. Am. Chem. Soc.* **2013**, *135*, 18774–18777.
- Tan, S.; Feng, H.; Ji, Y.; Wang, Y.; Zhao, J.; Zhao, A.; Wang, B.; Luo, Y.; Yang, J.; Hou, J. G. Observation of Photocatalytic Dissociation of Water on Terminal Ti Sites of TiO₂(110)-1 × 1 Surface. *J. Am. Chem. Soc.* **2012**, *134*, 9978–9985.
- Friend, C. M. Perspectives on Heterogeneous Photochemistry. *Chem. Rec.* **2014**, *14*, 944–951.
- Stevanovic, V.; Lany, S.; Ginley, D. S.; Tumas, W.; Zunger, A. Assessing capability of semiconductors to split water using ionization potentials and electron affinities only. *Phys. Chem. Chem. Phys.* **2014**, *16*, 3706–3714.
- Migani, A.; Mowbray, D. J.; Zhao, J.; Petek, H. Quasiparticle interfacial level alignment of highly hybridized frontier levels: H₂O on TiO₂(110). *J. Chem. Theory Comput.* **2015**, *11*, 239–251.
- Cheng, J.; VandeVondele, J.; Sprik, M. Identifying Trapped Electronic Holes at the Aqueous TiO₂ Interface. *J. Phys. Chem. C* **2014**, *118*, 5437–5444.
- Hedin, L. New Method for Calculating the One-Particle Green's Function with Application to the Electron-Gas Problem. *Phys. Rev.* **1965**, *139*, A796–A823.
- Onida, G.; Reining, L.; Rubio, A. Electronic excitations: density-functional versus many-body Green's-function approaches. *Rev. Mod. Phys.* **2002**, *74*, 601–659.
- Migani, A.; Mowbray, D. J.; Iacomino, A.; Zhao, J.; Petek, H.; Rubio, A. Level Alignment of a Prototypical Photocatalytic System: Methanol on TiO₂(110). *J. Am. Chem. Soc.* **2013**, *135*, 11429–11432.
- Migani, A.; Mowbray, D. J.; Zhao, J.; Petek, H.; Rubio, A. Quasiparticle level alignment for photocatalytic interfaces. *J. Chem. Theory Comput.* **2014**, *10*, 2103–2114.
- Migani, A.; Mowbray, D. J. Coverage dependence of the level alignment for methanol on TiO₂(110). *Comp. Theor. Chem.* **2014**, *1040–1041*, 259–265.
- De Angelis, F.; Di Valentin, C.; Fantacci, S.; Vittadini, A.; Selloni, A. Theoretical Studies on Anatase and Less Common TiO₂Phases: Bulk, Surfaces, and Nanomaterials. *Chem. Rev.* **2014**, *114*, 9708–9753.
- Lazzeri, M.; Vittadini, A.; Selloni, A. Structure and energetics of stoichiometric TiO₂ anatase surfaces. *Phys. Rev. B* **2001**, *63*, 155409.
- Yan, J.; Wu, G.; Guan, N.; Li, L.; Li, Z.; Cao, X. Understanding the effect of surface/bulk defects on the photocatalytic activity of TiO₂: anatase versus rutile. *Phys. Chem. Chem. Phys.* **2013**, *15*, 10978–10988.
- Brookes, I. M.; Murnyn, C. A.; Thornton, G. Imaging Water Dissociation on TiO₂(110). *Phys. Rev. Lett.* **2001**, *87*, 266103.
- Kurtz, R. L.; Stock-Bauer, R.; Madey, T. E.; Román, E.; Segovia, J. L. D. Synchrotron radiation studies of H₂O adsorption on TiO₂(110). *Surf. Sci.* **1989**, *218*, 178–200.
- Krischok, S.; Höfft, O.; Günster, J.; Stultz, J.; Goodman, D.; Kemper, V. H₂O interaction with bare and Li-precovered TiO₂: studies with electron spectroscopies (MIES and UPS(HeI and II)). *Surf. Sci.* **2001**, *495*, 8–18.
- Shishkin, M.; Kresse, G. Implementation and performance of the frequency-dependent GW method within the PAW framework. *Phys. Rev. B* **2006**, *74*, 035101.
- Shishkin, M.; Marsman, M.; Kresse, G. Accurate Quasiparticle Spectra from Self-Consistent GW Calculations with Vertex Corrections. *Phys. Rev. Lett.* **2007**, *99*, 246403.
- Perdew, J. P.; Zunger, A. Self-interaction correction to density-functional approximations for many-electron systems. *Phys. Rev. B* **1981**, *23*, 5048–5079.
- Perdew, J. P.; Burke, K.; Ernzerhof, M. Generalized Gradient Approximation Made Simple. *Phys. Rev. Lett.* **1996**, *77*, 3865.
- Heyd, J.; Scuseria, G. E.; Ernzerhof, M. Hybrid functionals based on a screened Coulomb potential. *J. Chem. Phys.* **2003**, *118*, 8207.
- Krukau, A. V.; Vydrov, O. A.; Izmaylov, A. F.; Scuseria, G. E. Influence of the exchange screening parameter on the performance of screened hybrid functionals. *J. Chem. Phys.* **2006**, *125*, 224106.
- Cheng, J.; Sprik, M. Alignment of electronic energy levels at electrochemical interfaces. *Phys. Chem. Chem. Phys.* **2012**, *14*, 11245–11267.
- Cheng, J.; Sprik, M. Aligning electronic energy levels at the TiO₂/H₂O interface. *Phys. Rev. B* **2010**, *82*, 081406.
- Chung, Y. W.; Lo, W. J.; Somorjai, G. A. Low energy electron diffraction and electron spectroscopy studies of the clean (110) and (100) titanium dioxide (rutile) crystal surfaces. *Surf. Sci.* **1977**, *64*, 588–602.
- Onishi, H.; Aruga, T.; Egawa, C.; Iwasawa, Y. Adsorption of CH₃OH, HCOOH and SO₂ on TiO₂(110) and stepped TiO₂(441) surfaces. *Surf. Sci.* **1988**, *193*, 33–46.
- Borodin, A.; Reichling, M. Characterizing TiO₂(110) surface states by their work function. *Phys. Chem. Chem. Phys.* **2011**, *13*, 15442–15447.
- Onda, K.; Li, B.; Petek, H. Two-photon photoemission spectroscopy of TiO₂(110) surfaces modified by defects and O₂ or H₂O adsorbates. *Phys. Rev. B* **2004**, *70*, 045415.
- Landmann, M.; Rauls, E.; Schmidt, W. G. The electronic structure and optical response of rutile, anatase and brookite TiO₂. *J. Phys.: Condens. Matter* **2012**, *24*, 195503.
- Marques, M. A. L.; Vidal, J.; Oliveira, M. J. T.; Reining, L.; Botti, S. Density-based mixing parameter for hybrid functionals. *Phys. Rev. B*

- 2011, 83, 035119.
- (48) Kresse, G.; Joubert, D. From ultrasoft pseudopotentials to the projector augmented-wave method. *Phys. Rev. B* **1999**, *59*, 1758.
- (49) Kresse, G.; Furthmüller, J. Efficient iterative schemes for ab initio total-energy calculations using a plane-wave basis set. *Phys. Rev. B* **1996**, *54*, 11169.
- (50) Yan, Q.; Rinke, P.; Winkelkemper, M.; Qteish, A.; Bimberg, D.; Scheffler, M.; de Walle, C. G. V. Band parameters and strain effects in ZnO and group-III nitrides. *Semi. Sci. Tech.* **2011**, *26*, 014037.
- (51) Botti, S.; Marques, M. A. L. Strong Renormalization of the Electronic Band Gap due to Lattice Polarization in the GW Formalism. *Phys. Rev. Lett.* **2013**, *110*, 226404.
- (52) Chiodo, L.; García-Lastra, J. M.; Iacolino, A.; Ossicini, S.; Zhao, J.; Petek, H.; Rubio, A. Self-energy and excitonic effects in the electronic and optical properties of TiO₂ crystalline phases. *Phys. Rev. B* **2010**, *82*, 045207.
- (53) Kang, W.; Hybertsen, M. S. Quasiparticle and optical properties of rutile and anatase TiO₂. *Phys. Rev. B* **2010**, *82*, 085203.
- (54) van Setten, M. J.; Gremaud, R.; Brocks, G.; Dam, B.; Kresse, G.; de Wijs, G. A. Optical response of the sodium alanate system: GW₀-BSE calculations and thin film measurements. *Phys. Rev. B* **2011**, *83*, 035422.
- (55) Reining, L.; Olevano, V.; Rubio, A.; Onida, G. Excitonic Effects in Solids Described by Time-Dependent Density-Functional Theory. *Phys. Rev. Lett.* **2002**, *88*, 066404.
- (56) Burdett, J. K.; Hughbanks, T.; Miller, G. J.; Richardson, J. W.; Smith, J. V. Structural-electronic relationships in inorganic solids: powder neutron diffraction studies of the rutile and anatase polymorphs of titanium dioxide at 15 and 295 K. *J. Am. Chem. Soc.* **1987**, *109*, 3639–3646.
- (57) Hammer, B.; Hansen, L. B.; Nørskov, J. K. Improved Adsorption Energetics within Density-Functional Theory Using Revised Perdew-Burke-Ernzerhof Functionals. *Phys. Rev. B* **1999**, *59*, 7413–7421.
- (58) Martínez, J. I.; Hansen, H. A.; Rossmeisl, J.; Nørskov, J. K. Formation energies of rutile metal oxides using density functional theory. *Phys. Rev. B* **2009**, *79*, 045120.
- (59) Calle-Vallejo, F.; Martínez, J. I.; García-Lastra, J. M.; Mogensen, M.; Rossmeisl, J. Trends in Stability of Perovskite Oxides. *Angew. Chem. Int. Ed.* **2010**, *49*, 7699–7701.
- (60) Zhu, T.; Gao, S.-P. The Stability, Electronic Structure, and Optical Property of TiO₂ Polymorphs. *J. Phys. Chem. C* **2014**, *118*, 11385–11396.
- (61) Tezuka, Y.; Shin, S.; Ishii, T.; Ejima, T.; Suzuki, S.; Sato, S. Photoemission and Bremsstrahlung Isochromat Spectroscopy Studies of TiO₂ (Rutile) and SrTiO₃. *J. Phys. Soc. Jpn.* **1994**, *63*, 347–357.
- (62) Reyes-Coronado, D.; Rodríguez-Gattorno, G.; Espinosa-Pesqueira, M. E.; Cab, C.; de Coss, R.; Oskam, G. Phase-pure TiO₂ nanoparticles: anatase, brookite and rutile. *Nanotechnology* **2008**, *19*, 145605.
- (63) Tang, H.; Lévy, F.; Berger, H.; Schmid, P. Urbach tail of anatase TiO₂. *Phys. Rev. B* **1995**, *52*, 7771–7774.
- (64) Amtout, A.; Leonelli, R. Optical properties of rutile near its fundamental band gap. *Phys. Rev. B* **1995**, *51*, 6842–6851.
- (65) Pascual, J.; Camassel, J.; Mathieu, H. Fine structure in the intrinsic absorption edge of TiO₂. *Phys. Rev. B* **1978**, *18*, 5606–5614.
- (66) Hosaka, N.; Sekiya, T.; Satoko, C.; Kurita, S. Optical Properties of Single-Crystal Anatase TiO₂. *J. Phys. Soc. Jpn.* **1997**, *66*, 877–880.
- (67) Lee, B.; Ki Lee, C.; Hwang, C. S.; Han, S. Influence of exchange-correlation functionals on dielectric properties of rutile TiO₂. *Curr. Appl. Phys.* **2011**, *11*, S293–S296.
- (68) Cardona, M.; Harbeke, G. Optical Properties and Band Structure of Wurtzite-Type Crystals and Rutile. *Phys. Rev.* **1965**, *137*, A1467–A1476.
- (69) Tiwald, T. E.; Schubert, M. Measurement of rutile TiO₂ dielectric tensor from 0.148 to 33 μm using generalized ellipsometry. *Proc. SPIE* **2000**, *4103*, 19–29.
- (70) Traylor, J. G.; Smith, H. G.; Nicklow, R. M.; Wilkinson, M. K. Lattice Dynamics of Rutile. *Phys. Rev. B* **1971**, *3*, 3457–3472.
- (71) Bruneval, F.; Marques, M. A. L. Benchmarking the Starting Points of the GW Approximation for Molecules. *J. Chem. Theory Comput.* **2013**, *9*, 324–329.
- (72) Pfeifer, V.; Erhart, P.; Li, S.; Rachut, K.; Morasch, J.; Brötz, J.; Reckers, P.; Mayer, T.; Rühle, S.; Zaban, A.; Mora Seró, I.; Bisquet, J.; Jaegermann, W.; Klein, A. Energy Band Alignment between Anatase and Rutile TiO₂. *J. Phys. Chem. Lett.* **2013**, *4*, 4182–4187.
- (73) Scanlon, D. O.; Dunnill, C. W.; Buckeridge, J.; Shevlin, S. A.; Logsdail, A. J.; Woodley, S. M.; Catlow, C. R. A.; Powell, M. J.; Palgrave, R. G.; Parkin, I. P.; Watson, G. W.; Keal, T. W.; Sherwood, P.; Walsh, A.; Sokol, A. A. Band alignment of rutile and anatase TiO₂. *Nat. Mater.* **2013**, *12*, 798–801.
- (74) Sanches, F. F.; Mallia, G.; Liborio, L.; Diebold, U.; Harrison, N. M. Hybrid exchange density functional study of vicinal anatase TiO₂ surfaces. *Phys. Rev. B* **2014**, *89*, 245309.
- (75) Cheng, J.; Sulpizi, M.; VandeVondele, J.; Sprik, M. Hole Localization and Thermochemistry of Oxidative Dehydrogenation of Aqueous Rutile TiO₂(110). *ChemCatChem* **2012**, *4*, 636–640.
- (76) Selloni, A.; Vittadini, A.; Gräzel, M. The adsorption of small molecules on the TiO₂ anatase (101) surface by first-principles molecular dynamics. *Surf. Sci.* **1998**, *402*, 219–222.
- (77) He, Y.; Tilocca, A.; Dulub, O.; Selloni, A.; Diebold, U. Local ordering and electronic signatures of submonolayer water on anatase TiO₂(101). *Nat. Mater.* **2009**, *8*, 585–589.
- (78) Herman, G. S.; Dohnálek, Z.; Ruzyccki, N.; Diebold, U. Experimental Investigation of the Interaction of Water and Methanol with Anatase–TiO₂(101). *J. Phys. Chem. B* **2003**, *107*, 2788–2795.
- (79) Lee, J.; Sorescu, D. C.; Deng, X.; Jordan, K. D. Water Chain Formation on TiO₂(110). *J. Phys. Chem. Lett.* **2013**, *4*, 53–57.
- (80) Kimmel, G. A.; Baer, M.; Petrik, N. G.; VandeVondele, J.; Rousseau, R.; Mundy, C. J. Polarization- and Azimuth-Resolved Infrared Spectroscopy of Water on TiO₂(110): Anisotropy and the Hydrogen-Bonding Network. *J. Phys. Chem. Lett.* **2012**, *3*, 778–784.
- (81) Liu, L.-M.; Zhang, C.; Thornton, G.; Michaelides, A. Structure and dynamics of liquid water on rutile TiO₂(110). *Phys. Rev. B* **2010**, *82*, 161415.
- (82) Zhao, J.; Li, B.; Jordan, K. D.; Yang, J.; Petek, H. Interplay between hydrogen bonding and electron solvation on hydrated TiO₂(110). *Phys. Rev. B* **2006**, *73*, 195309.
- (83) Onda, K.; Li, B.; Zhao, J.; Jordan, K. D.; Yang, J.; Petek, H. Wet Electrons at the H₂O/TiO₂(110) Surface. *Science* **2005**, *308*, 1154–1158.
- (84) Mowbray, D. J.; Martínez, J. I.; Calle-Vallejo, F.; Rossmeisl, J.; Thygesen, K. S.; Jacobsen, K. W.; Nørskov, J. K. Trends in Metal Oxide Stability for Nanorods, Nanotubes, and Surfaces. *J. Phys. Chem. C* **2011**, *115*, 2244–2252.
- (85) Tritsarlis, G. A.; Vinichenko, D.; Kolesov, G.; Friend, C. M.; Kaxiras, E. Dynamics of the Photogenerated Hole at the Rutile TiO₂(110)/Water Interface: A Nonadiabatic Simulation Study. *J. Phys. Chem. C* **2014**, *118*, 27393–27401.
- (86) Xu, C.; Yang, W.; Guo, Q.; Dai, D.; Chen, M.; Yang, X. Molecular Hydrogen Formation from Photocatalysis of Methanol on Anatase-TiO₂(101). *J. Am. Chem. Soc.* **2014**, *136*, 602–605.
- (87) Luttrell, T.; Halpegamage, S.; Tao, J.; Kramer, A.; Sutter, E.; Batzill, M. Why is anatase a better photocatalyst than rutile? - Model studies on epitaxial TiO₂ films. *Sci. Rep.* **2014**, *4*, 4043.
- (88) Schaub, R.; Thostrup, P.; Lopez, N.; Laegsgaard, E.; Stensgaard, I.; Nørskov, J. K.; Besenbacher, F. Oxygen Vacancies as Active Sites for Water Dissociation on Rutile TiO₂(110). *Phys. Rev. Lett.* **2001**, *87*, 266104.
- (89) Aschauer, U.; He, Y.; Cheng, H.; Li, S.-C.; Diebold, U.; Selloni, A. Influence of Subsurface Defects on the Surface Reactivity of TiO₂: Water on Anatase (101). *J. Phys. Chem. C* **2010**, *114*, 1278–1284.
- (90) Li, Y.; Gao, Y. Interplay between Water and TiO₂ Anatase (101) Surface with Subsurface Oxygen Vacancy. *Phys. Rev. Lett.* **2014**, *112*, 206101.
- (91) Aschauer, U.; Selloni, A. Hydrogen interaction with the anatase TiO₂(101) surface. *Phys. Chem. Chem. Phys.* **2012**, *14*, 16595–16602.
- (92) Setvin, M.; Franchini, C.; Hao, X.; Schmid, M.; Janotti, A.; Kaltak, M.; Van de Walle, C. G.; Kresse, G.; Diebold, U. Direct View at Excess Electrons in TiO₂ Rutile and Anatase. *Phys. Rev. Lett.* **2014**, *113*, 086402.
- (93) Minato, T.; Sainoo, Y.; Kim, Y.; Kato, H. S.; Aika, K.-i.; Kawai, M.; Zhao, J.; Petek, H.; Huang, T.; He, W.; Wang, B.; Wang, Z.; Zhao, Y.; Yang, J.; Hou, J. G. The electronic structure of oxygen atom vacancy and hydroxyl impurity defects on titanium dioxide (110) surface. *J. Chem. Phys.* **2009**, *130*, 124502.
- (94) Papageorgiou, A. C.; Beglitis, N. S.; Pang, C. L.; Teobaldi, G.; Cabailh, G.; Chen, Q.; Fisher, A. J.; Hofer, W. A.; Thornton, G. Electron traps and their effect on the surface chemistry of TiO₂(110). *Proc. Natl. Acad. Sci.* **2010**, *107*, 2391–2396.
- (95) Thomas, A. G.; Flavell, W. R.; Mallick, A. K.; Kumarasinghe, A. R.; Tsoutsou, D.; Khan, N.; Chatwin, C.; Rayner, S.; Smith, G. C.; Stockbauer, R. L.; Warren, S.; Johal, T. K.; Patel, S.; Holland, D.; Taleb, A.; Wiame, F. Comparison of the electronic structure of anatase and rutile TiO₂ single-crystal surfaces using resonant photoemission and x-ray absorption spectroscopy. *Phys. Rev. B* **2007**, *75*, 035105.
- (96) Argondizzo, A.; Cui, X.; Wang, C.; Sun, H.; Shang, H.; Zhao, J.; Petek, H. Ultrafast multiphoton pump-probe photoemission excitation pathways in rutile TiO₂(110). *Phys. Rev. B* **2015**, *91*, 155429.
- (97) Fujimori, A.; Bocquet, A.; Morikawa, K.; Kobayashi, K.; Saitoh, T.; Tokura, Y.; Hase, I.; Onoda, M. Electronic structure and electron-phonon interaction in transition metal oxides with d⁰ configuration and lightly doped compounds. *J. Phys. Chem. Solids* **1996**, *57*, 1379–1384.
- (98) Nørskov, J. K.; Rossmeisl, J.; Logadottir, A.; Lindqvist, L.; Kitchin, J. R.; Bligaard, T.; Jónsson, H. Origin of the Overpotential for Oxygen Reduction at a Fuel-Cell Cathode. *J. Phys. Chem. B* **2004**, *108*, 17886–17892.
- (99) Tilocca, A.; Selloni, A. Vertical and Lateral Order in Adsorbed Water Layers on Anatase TiO₂(101). *Langmuir* **2004**, *20*, 8379–8384.
- (100) Tilocca, A.; Selloni, A. Structure and Reactivity of Water Layers on Defect-Free and Defective Anatase TiO₂(101) Surfaces. *J. Phys. Chem. B* **2004**, *108*, 4743–4751.
- (101) Zhao, Z.; Li, Z.; Zou, Z. Structure and Properties of Water on the Anatase TiO₂(101) Surface: From Single-Molecule Adsorption to Interface Formation. *J. Phys. Chem. C* **2012**, *116*, 11054–11061.
- (102) Tilocca, A.; Selloni, A. Reaction pathway and free energy barrier for defect-induced water dissociation on the (101) surface of TiO₂-anatase. *J. Chem. Phys.* **2003**, *119*, 7445–7450.